Disruptive Role of Vertical Land Motion in Future Assessments of Climate Change-Driven Sea Level Rise and Coastal Flooding Hazards in the Chesapeake Bay.

[1*]Sonam Futi Sherpa, [1]Manoochcher Shirzaei and [2]Chandrakanta Ojha

[1]Virginia Tech, Department of Geosciences, Blacksburg, VA

[2]Department of Earth and Environmental Sciences, IISER Mohali, Punjab, India

*Corresponding Author

Keypoints

- We quantify 21st-century inundation hazards due to sea level rise, storm surge, and land subsidence combining space-based techniques.
- By 2100, inundated areas from sea level rise, and storm surges increases to 849-1117 km^2 for Shared Socioeconomic Pathways 1-1.9 to 5-8.5.
- Islands, wetlands, and National wildlife refuges flooded in even very low and low emissions scenarios such as SSPs 1-1.9-1-2.6.

Abstract

Future projections of sea-level rise used to assess coastal flooding hazards and exposure throughout the 21st century and devise risk mitigation efforts often lack an accurate estimate of coastal Vertical Land Motion (VLM) rate, driven by anthropogenic and non-climate factors in addition to climatic factors. The Chesapeake Bay (CB) region of the United States is experiencing one of the fastest rates of relative sea-level rise on the Atlantic coast of the United

States. This study uses a combination of space-borne Interferometric SAR (InSAR), Global Navigation Satellite System (GNSS), Light Detecting and Ranging (LIDAR) datasets, available National Oceanic and Atmospheric Administration (NOAA) long term tide gauge data, and sea-level rise projections from the Intergovernmental Panel on Climate Change (IPCC), AR6 WG1 to quantify the regional rate of RSLR and future flooding hazards for the years 2030, 2050, and 2100. By the year 2100, the total inundated areas from SLR and subsidence are projected to be 454-600 km^2 for Shared Socioeconomic Pathways (SSPs) 1-1.9 to 5-8.5 respectively and 343-627 km^2 only from SLR. The effect of storm surges based on Hurricane Isabel can increase the inundated area to 849-1117 km^2 under different VLM and SLR scenarios. We present that accurate estimates of VLM rate, such as those obtained here, are essential to revise IPCC projections and obtain accurate maps of coastal flooding and inundation hazards. The results provided here inform policymakers when assessing hazards associated with global climate changes and local factors in CB, required for developing risk management and disaster resilience plans.

Keywords: Sea level rise, Solid Earth Change, Climate Projections, Future Coastal Inundation and hazards, Disaster Resilience, Climate Change

Plain Language Summary

The Chesapeake Bay region of the United States is experiencing one of the fastest rates of relative sea-level rise on the Atlantic coast of the United States. However, future projections of sea-level rise used to assess coastal flooding hazards and exposure throughout the 21st century often lack an accurate estimate of changes in sea level relative to land. This poses a significant challenge to present and future management efforts and plans as it undermines flooding in coastal communities. In this work, we combine satellite techniques and ground measurement to obtain vertical land motion to assess twenty first century flooding hazards due to Sea Level Rise, Hurricane effect, and land movement in the Chesapeake Bay. By the year 2100, the total inundated areas from sea-level rise and subsidence are projected to be 454-600 km^2 for very low to very high greenhouse gas scenarios respectively. The effect of storm surges based on Hurricane Isabel can increase the inundated area to 849-1117 km^2 under different changes in vertical land movement and sea-level rise scenarios. The results provided here inform policymakers when assessing hazards associated with global climate changes and local factors.

1. Introduction

Rising sea levels pose significant challenges to coastal communities and ecosystems (IPCC, 2021). The global sea level rose by 0.20 m between 1901 and 2018, with an average rate of 1.3 mm/year between 1901 and 1971, increasing to 1.9 mm/year between 1971-2006 and further increasing to 3.7 mm/year between 2006 and 2018 with high confidence (IPCC, 2021). This acceleration will likely continue throughout the 21st century (Dangendorf et al., 2019; Frederikse et al., 2020; Nerem et al., 2018). However, on a local scale, the rate of regional sea-level change could be larger than the average global sea-level change due to processes that affect vertical land motions such as groundwater pumping/recharge, sediment compaction, hydrologic loading, long term tectonics, Glacial Isostatic Adjustment (GIA), dynamic topography, and sediment loading (Manoochehr Shirzaei et al., 2021). To quantify the impacts of relative Sea-Level Rise (RSLR) on coastal flooding, socioeconomic exposures, and risks, it is crucial to obtain accurate Vertical Land Motion (VLM) rates at management-relevant resolution (10 s m^2) (Blackwell et al., 2020; Manoochehr Shirzaei et al., 2017). Relative sea-level change refers to sea surface changes over time concerning a local land elevation in response to changing climate and local non-tectonic and anthropogenic processes.

Several studies have highlighted sea level rise in coastal Virginia waters and have identified it as a hotspot for rising sea-level due to climate variability and global warming (Davis & Vinogradova, 2017; Ezer & Corlett, 2012; Sallenger et al., 2012). On the land side, recent studies (Bekaert et al., 2017; Buzzanga et al., 2020; Harvey et al., 2021; Karegar et al., 2017) showed that the Hampton Roads area of the Chesapeake Bay region (Fig. 1) is experiencing subsidence and suggested GIA and aquifer compaction as primary drivers (Eggleston & Pope, 2013). The

mid-Atlantic region's bedrock is slowly moving downward in response to the melting of the Laurentide ice sheet that covered Canada and the northern United States during the last ice (Sella et al., 2007; J. Boon et al., 2010), generating ~1-2 mm/year of subsidence (Peltier et al., 2018). Further, the region hosts the Coastal Plain Aquifer system comprising unconsolidated sediments overlaying the eastward dipping Precambrian basement (McFarland & Scott, 2006). The Potomac Aquifer, the largest and deepest unit among different layers, is the primary source of freshwater supply in eastern Virginia. As a result, pumping has caused the groundwater level to decline by more than 60 m in some regions, manifesting in localized and rapid land subsidence (Bekaert et al., 2017). Currently, the Sustainable Water Initiative for Tomorrow (SWIFT) project designed by Virginia authorities actively recharge replenishes the Potomac Aquifer with up to one million gallons of drinking water daily to enhance freshwater's long-term sustainability and offset the land subsidence.

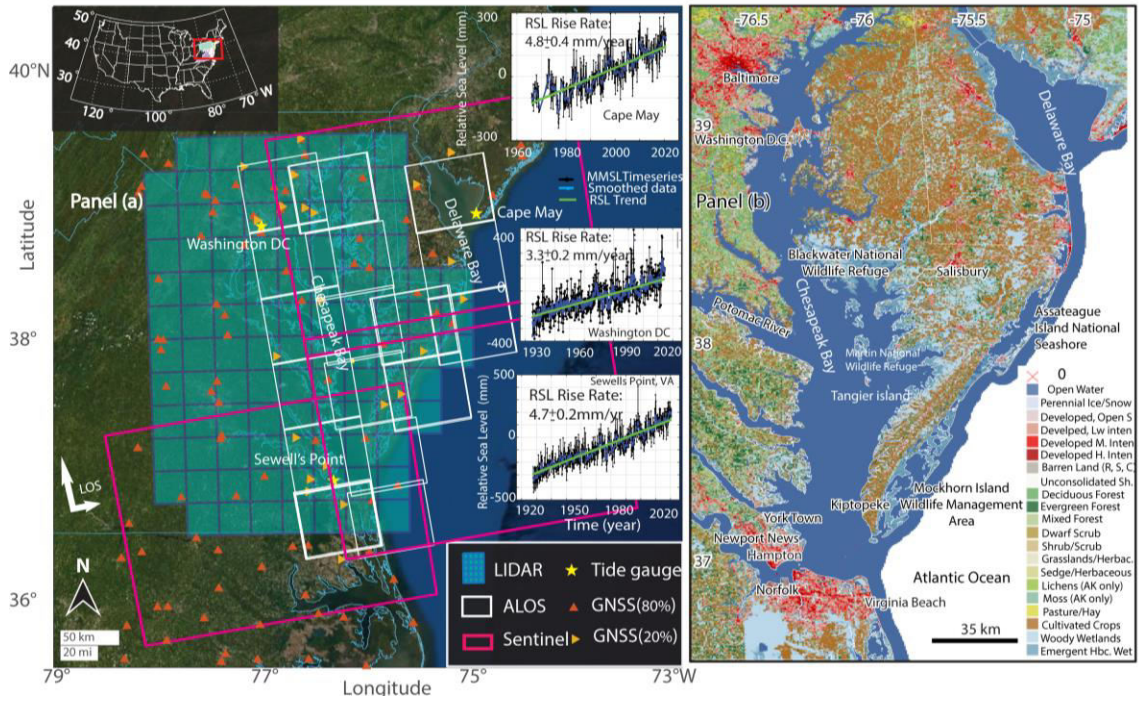

Figure.1. Chesapeake Bay Study Area. **(a)**, shown are the ground footprint of SAR satellites frames, Sentinel-1 A/B, C-band (Magenta) and ALOS PALSAR L-band (white), location of tide gauges (yellow

stars), GNSS stations (80%) used in the analysis (orange triangle) and 20% of GNSS (yellow triangles) used for VLM validation. Further, time-series data of Monthly Mean Sea Level (MMSL) (average of high tides and low tides) from NOAA (National Oceanic and Atmospheric Administration) for three stations, Sewell's Point, VA, Washington DC, and Cape May, are shown. **(b)** shows Landsat-based 30 m resolution land use and landcover area for the study area (Homer et al., 2012).

Chesapeake Bay region is affected by combined flooding from ocean dynamics of the Gulf Stream and Atlantic Meridional Overturning Circulation (Ezer & Corlett, 2012), tidal flooding (Sweet & Park, 2014), and documented increasingly extreme rainfall (Allen & Allen, 2019). On the other hand, increased inundation hazards due to storm surges on the Chesapeake Bay are demonstrated in various studies (Cho et al., 2012; Shen et al., 2006; Sheng et al., 2010). On September 18, 2003, a category 2 Hurricane Isabel made landfall over the mid-Atlantic region generating record conditions for the region's 27 years of monitoring and impact (Smith & Graffeo, 2005), resulting in a historical maximum water level records at eight stations in the Chesapeake Bay (Hovis et al., 2004). On 2012 October 29, Hurricane Sandy (category 1), an Atlantic hurricane on record, made landfall on a long swath of the U.S. Atlantic coastline, including the Chesapeake Bay (Sopkin et al., 2014), with a damaging storm surge imparted to the New Jersey and New York coastlines (Blake et al., 2013). The maximum recorded storm surge from National Oceanic and Atmospheric Administration (NOAA) ranked by amplitude for Hurricane Isabel, September 2003 and Hurricane Sandy, October 2012 is reported in Table 1, which shows that Sewell's Point, Cape May station, and Washington DC experienced a water level of 1.7, 1.0 and 2.4 meters (for Hurricane Isabel) and 1.4, 1.6, and 1.2 meters respectively (for Hurricane Sandy). Further, some areas such as the City of Norfolk already experience "sunny days" or nuisance flooding regularly when there is a high tide or a storm offshore,

without a named storm event on land. These increasingly frequent flooding events will require regional and local planning for both evacuations in the face of extreme storm events and longer-term adaptation.

Table 1. Maximum recorded storm surge ranked by amplitude for Hurricane Sandy, recorded in October 2012 (Source: Fanelli et al., 2013, table 3a), and maximum storm surge for Hurricane Isabel (Source: Hovis et al., 2004, table 3-4) recorded on 18-19 September 2003 (meters) at three stations of Chesapeake Bay.

Hurricane	Station Name	Station ID	Date and Time (GMT)	Water level (meters)
Sandy	Sewell's Point, VA	8638610	10/29/2012 07:24	1.394
	Cape May, NJ	8536110	10/29/2012 18:00	1.574
	Washington, DC	8594900	10/30/2012 21:42	1.228
Isabel	Sewell's Point, VA	8638610	09/18/2003 21:00	1.712
	Cape May, NJ	8536110	09/18/2003 23:48	0.951
	Washington, DC	8594900	09/19/2003 09:30	2.470

Space geodetic tools, including Interferometric Synthetic Aperture Radar (InSAR) and Global Navigation System Satellites (GNSS), can measure the movement of the land surface at a millimeter level accuracy (Bürgmann et al., 2000) which is essential in understanding change in relative SLR rate. Such observations improve the understanding of long-term changes in relative sea level. The usefulness of space-based InSAR and GNSS observation are discussed in various studies on earth deformation in the Chesapeake Bay (Bekaert et al., 2017; Buzzanga et al., 2020). However, these studies only focused on short observation periods, spanned by ALOS or a

portion of Sentinel-1A/B acquisitions, thus yielding a lower signal-to-noise ratio for the long-term rates. Also, their estimates of the VLM rate are not tied to a reference frame, so they are not suitable for studies of SLR and flooding hazards.

We apply a framework to combine the entire archive of Sentinel-1 and ALOS SAR satellites and GNSS observations to obtain spatially and temporally high-resolution VLM maps and improve their uncertainties. We further evaluate future flooding and inundation hazards extents by combining VLM rates with the LiDAR topographic dataset, SLR projections under different Shared Socioeconomic Pathways (SSPs) scenarios, and storm surge estimates from Hurricane Sandy and Isabel for time period 2030-2100. High-resolution VLM rates with mm-level accuracy, improved forecasts of relative SLR rates, and updated maps of inundation hazards are essential for informing policymakers and authorities and developing flood resiliency plans to compact severe consequences of climate change in the region.

2. Datasets and Methods

2.1.Tide Gauge Data

We used National Oceanic and Atmospheric Administration (NOAA) tide gauges to understand the water level changes in the Chesapeake Bay (Fig. 1). The tide gauge data were obtained from the NOAA website https://tidesandcurrents.noaa.gov/map/index.html. A combined total of 254 years of water level measurements with record lengths varying between 93 years (1927-2020) at the Sewell's Point (8638610), VA, 96 years (1924-2020) at the Washington DC station (8594900), and 55 years (1965-2020) at the Cape May site (8536110) are available. The monthly mean sea level heights recorded at the U.S. tide stations are verified for their accuracy through National Water Level Observation Network (NWLON) quality control procedures. They are referenced to *Mean Sea Level* (MSL), a tidal datum specifically defined in

and for the U.S. following Federal law (Gill & Schultz, 2001). Linear trend analysis of the monthly mean sea level (MMSL) data from these three stations adjacent to or within SAR frames showed a relative sea-level of 4.7± 0.2 mm/year at Sewell's Point, 3.3± 0.2 mm/year, and 4.8 ± 0.4 mm/year at Washington D.C. and Cape May stations respectively (Fig.1). A study by Boon (2018) has also shown increasing regional sea level using a quadratic model among coastal regions. The MMSL data refers to the water level observed over a calendar month at U.S. tide stations.

2.2. SAR and GNSS Datasets

To obtain a map of high-resolution VLM with respect to a global reference frame and mm-level precision, we applied the framework shown in Fig. 2 to combine all available SAR and GNSS observations. In the following, we detail different components of this framework.

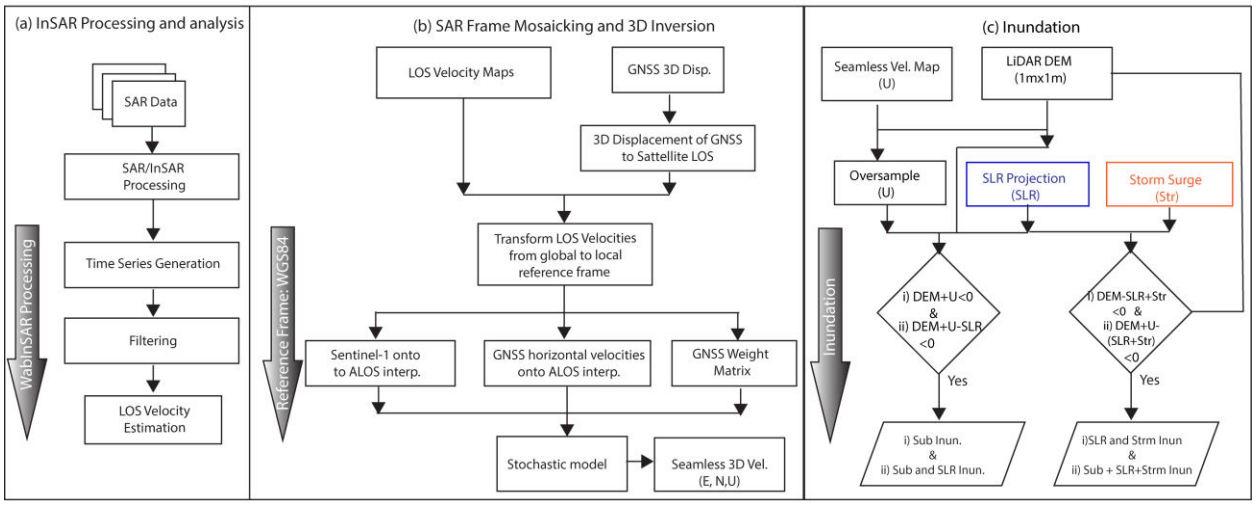

Figure 2. Methodology flowchart. **(a)** The InSAR multitemporal processing and line of sight (LOS) rate estimation, **(b)** Mosaicking and 3D inversion of InSAR and GNSS datasets, **(c)** Flooding and inundation hazard estimation from subsidence, sea-level rise, and storm surge.

169

170 **2.1.1. Interferogram Generation and Time Series Analysis**

171 To measure vertical land motion in the Chesapeake Bay, a large set of SAR images acquired
172 by C-band Sentinel-1 with Terrain Observation with Progressive Scans acquisition mode
173 (Interferometric Wide Swath -IW mode) with a revisit time of twelve days and the Advanced
174 Land Observing Satellite (ALOS) Phased Array L-band Synthetic Aperture Radar (PALSAR) L-
175 band with a revisit time of 46 days in ascending orbit geometry from 2007-2020 were used. We
176 used a multi-looking factor of 32 and 6 in range and azimuth direction and yielded pixel
177 resolution of ~75 m × ~84 m for Sentinel-1 and a muti-looking factor of 4 and 13 in range and
178 azimuth direction, leading to approximately ~50 x ~50 m for ALOS satellite for vertical land
179 motion estimation leading to the ultimate resolution of ~50 x ~50 m. The list of acquisitions is
180 provided in table S1. Here, a level-1 data format was used, including SLC products, orbits, and
181 calibration XML files.

182 We utilized Gamma processing software (Wegnüller et al., 2016; Werner et al., 2000) for
183 SAR processing and calibration, encompassing preprocessing, range compression, azimuth
184 compression, and multi-look post-processing modules. For multitemporal analysis of the
185 Sentinel-1 TOPS SAR data, we used the wavelet-based InSAR algorithm (Shirzaei, 2013;
186 Shirzaei et al., 2017). All SAR images were co-registered and resampled concerning a common
187 reference image (an image with the shortest temporal and spatial baselines and doppler
188 difference concerning the rest of the datasets) and generated large sets of interferograms.
189 Temporal and perpendicular baselines of 700 days and 500 m were used for the sentinel-1
190 dataset and 1500 days and 2500 m for ALOS. Here Shuttle Radar Topography Mission (SRTM)

version 3-1 arcsec (30 m) DEM and satellite precise ephemeris data were used to calculate and remove the geometrical phase (Franceschetti & Lanari, 1999). Following Shirzaei (2013), less noisy pixels (i.e., elite pixels) were selected through statistical analysis of complex interferometric phase noise time series. To reduce the effects of the residual DEM error, we applied a low pass filter before phase unwrapping. To obtain th absolute phase changes at for each elite pixel, we applied the sparse phase unwrapping algorithm (Costantini & Rosen, 1999) using the minimum cost flow approach (Costantini, 1998). To estimate and remove the effect of a topography correlated component of atmospheric delay, we applied the approach of Shirzaei and Bürgmann (2012). Also, each unwrapped interferogram was corrected for the effect of orbital error following (Manoochehr Shirzaei & Walter, 2011). Next, each elite pixel's time series of phase change/velocities was estimated through an iterative reweighted least squares. In this step, the initial observation weight matrix is estimated based on interferometric coherence. Next, a wavelet-based high-pass filter is applied to reduce the temporal component of the atmospheric delay in the time series. The location of the less noisy pixels was then transformed to a geographic coordinate system (WGS84) from a radar coordinate system. And lastly, linear line-of-sight (LOS) velocity is estimated for each pixel with respect to a reference point.

2.1.2. SAR frame mosaicking

To obtain two seamless LOS velocity maps for Sentinel-1 and ALOS frames, SAR frames are mosaiced following Ojha et al. (2018). To this end, we used pixels within overlapped areas of adjacent frames as tie points. We implemented an affine transformation (including translation and two rotations) to align datasets and ultimately obtain seamless LOS velocity maps for all tracks covering the Chesapeake Bay.

Next, we obtain GNSS observations from the study area, provided by Nevada Geodetic Laboratory with respect to IGS14 reference frame (Blewitt et al., 2018). Data from 99 stations, whose observations date to 2007 with minimum lengths greater than three years, were obtained. After applying relevant corrections (such as step correction), we estimate trends using a robust regression and refine the vertical velocity field using a median filter, following (Hammond et al., 2016). We randomly split the dataset into sets of 80% (tie) and 20% (check) stations. The check stations were not used in the analysis and only kept for validating results. The tie datasets used to constrain parameters of an affine transformation to convert LOS velocities from local to the global reference frame. To this end, we projected 3D displacement velocities from GNSS onto satellite LOS direction using local incidence and heading angle of the satellite and then applied an affine transformation. Figures 3 A and B show the seamless maps of LOS rate for ALOS and Sentinel-1, respectively.

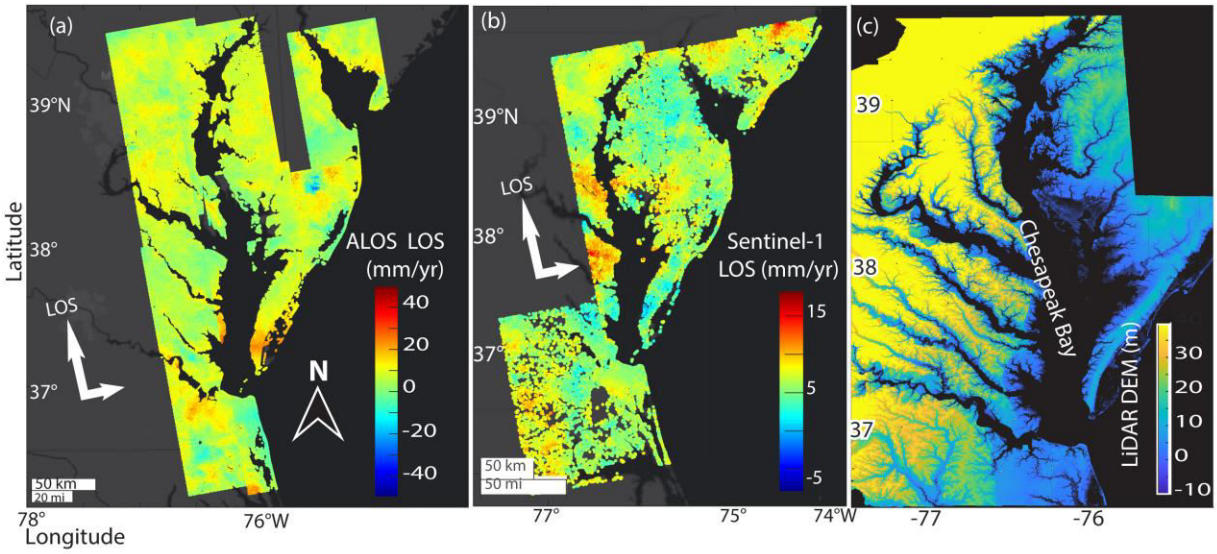

Figure 3. Mosaiced ALOS LOS rate **(a),** Mosaiced Sentinel-1 LOS rate **(b)** Lidar DEM **(c)**.

2.1.3. 3D displacement rate inversion

Next, we interpolated the LOS velocities and standard deviations of Sentinel-1 track and GNSS horizontal velocities on the location of ALOS pixels, using a Kriging interpolation approach with inverse distance weighting (Trochu, 1993), resulting in four observations per pixel, including two LOS velocities and two GNSS velocities (E-W and N-S components) with three unknowns, including velocities in the east (E), north (N) and up (U).

The interpolated GNSS east and north standard deviations, σ^e and σ^n for interpolated values is modeled based on their distance (D) to the nearest GNSS station as follows;

$$\sigma^e = s_e * \left(1 + \frac{D}{10}\right)$$
$$\sigma^n = s_n * \left(1 + \frac{D}{10}\right) \quad (1)$$

where, s_e and s_n are the standard deviation of GNSS station located at a distance of D km to a given pixel.

Provided interpolated LOS velocities and variances for a given pixel namely $\{y_{sa}, y_{aa}\}, and\ \{\sigma_{sa}^2, \sigma_{aa}^2\}$ respectively, with a subscript indicating Sentinel-1 ascending (sa) and ALOS ascending (aa), we implement the following stochastic model to generate a seamless, high spatial resolution map of the east (E), north (N), and vertical (U):

$$y_{sa} = C_e^{sa}E + C_n^{sa}N + C_u^{sa}U + \varepsilon^{sa}$$
$$y_{aa} = C_e^{aa}E + C_n^{aa}N + C_u^{aa}U + \varepsilon^{aa}$$
$$E_G = E + \varepsilon^e$$
$$N_G = N + \varepsilon^n \quad (2)$$

Here, C represents the unit vectors projecting the 3D displacements onto the LOS (Hanssen, 2001). The interpolated GNSS velocities in the E-W and N-S directions are E_G, and N_G. ε is the observations error with N (0, σ) probability distribution (σ is the SD). Note that in equation 2, E and N are unknown while E_G, and N_G are observed.

Solution to equation 1 is obtained as below:

$$X = (A^T PA)^{-1} A^T \mathrm{PL} \quad (3)$$

where,

$$X = (E\ N\ U)^T, \quad (4)$$

$$\mathrm{A}=\begin{pmatrix} C_e^{sa} & C_n^{sa} & C_u^{sa} \\ C_e^{aa} & C_n^{aa} & C_u^{aa} \\ 1 & 0 & 0 \\ 0 & 1 & 0 \end{pmatrix}, \quad (5)$$

$$P=\begin{pmatrix} \frac{1}{(\sigma^{sa})^2} & 0 & 0 & 0 \\ 0 & \frac{1}{(\sigma^{aa})^2} & 0 & 0 \\ 0 & 0 & \frac{1}{(\sigma^{e})^2} & 0 \\ 0 & 0 & 0 & \frac{1}{(\sigma^{n})^2} \end{pmatrix} \quad (6)$$

The parameter variance-covariance matrix is $Q_{xx} = \sigma_u^2\ (A^T PA)^{-1}$, where $\sigma_u^2 = \frac{r^T Pr}{n-u}$, $r = L - Ax, n$ is the number of equations and u is the number of unknowns. Combining of ALOS and Sentinel-1 datasets, allowed us to increase our redundancy, thus refining errors.

2.2. LiDAR Dataset

Next, we obtained a Light Detection and Ranging (LiDAR) elevation model a 1m × 1m resolution for Chesapeake Bay from the United States Geological Society (OCM Partners, 2021) (Fig.3 C). The 2016 USGS CoNED (Coastal National Elevation Database) Topo bathymetric Model (1859-2015): Chesapeake Bay dataset were obtained as a raster digital elevation model with vertical accuracy of 30 cm and horizontal accuracy of 100 cm with vertical Datum NAVD88 (North American Vertical Datum of 1988). This data has a temporal range of the input topography of 1859 to 2015.

The vertical land motion rates obtained in section 2.2.3 are resampled on this LiDAR DEM that is referred to the geographic coordinate system. We then adjust the DEM to incorporate subsidence projection following the assumption of a linear rate for the VLM during 21st century (Manoochehr Shirzaei et al., 2021). We subject the adjusted elevation model for VLM projections to multiple SLR and storm surge scenarios by subtracting the height of the transformed DEM from the SLR projection height (Figure 3C). A similar approach is used in Miller and Shirzaei (2021).

2.3. IPCC SLR Scenarios from AR6

We use future SLR scenarios from the latest Sixth Assessment Report (AR6) (Fox-Kemper et al., 2021; Garner et al., 2021, Garner et al., In prep) following SSPs (O'Neill et al., 2014; Riahi et al., 2017) adopted by the IPCC for projection periods of 2030, 2050 till 2100, relative to a baseline of 1995-2014 with medium confidence. In AR6 scenarios, a broader range of emissions futures is covered than considered in fifth assessment report, AR5, including high CO_2 emissions scenarios without climate change mitigation as well as a low CO_2 emissions scenario reaching net zero CO_2 emissions around mid-century (IPCC, 2021). SSPs scenarios offer a more

287 comprehensive assessment of climate drivers and responses and offer unprecedented detail of
288 input data for Earth System Model (ESM) simulations than in the Representative Concentration
289 Pathways (RCPs) used in the AR5 (IPCC, 2021).

290 SLR projections account for contributions from global processes such as melting of the
291 Greenland Ice Sheet (GIS), Antarctic Ice sheet (AIS), land water storage changes, and
292 Sterodynamic processes, as well as long-wavelength vertical land motion signals due to Glacial
293 Isostatic Adjustment (GIA). A detailed description of the process is found in IPCC AR6 report
294 Box 9.1 (Fox-Kemper et al., 2021). We use the 50^{th} percentiles (i.e., median) projections for
295 different SLR scenarios of SSP1-1.9, SSP1-2.6, SSP2-4.5, SSP3-7.0, and SSP5-8.5 at the
296 location of three tide gauge stations within the Chesapeake Bay area, including Sewell's Point,
297 Cape May, and Washington DC (Table 2) to investigate inundation hazards. Here, SSP3-7.0 and
298 SSP5-8.5 indicate high and very high greenhouse gas (GHG) emissions and CO_2 emissions that
299 roughly double from current levels by 2100 and 2050, respectively, SSP2-4.5 is scenarios with
300 intermediate GHG emissions and CO_2 emissions remaining around current levels until the middle
301 of the century, and SSP1-1.9 and SSP1-2.6 represent scenarios with very low and low GHG
302 emissions and CO_2 emissions declining to net zero around or after 2050, followed by varying
303 levels of net negative CO_2 emissions (IPCC, 2021, Summary for Policy Maker, Box SPM 1). The
304 details of each SSPs are provided at the header of table 2.

305 For our analysis, we obtained the SLR projections without the effect of VLM as well as
306 SLR due only to the effect of VLM. The former is used in combination with our measured VLM
307 rates to investigate inundation hazards in the region, while the latter is used to assess the
308 accuracy of VLM rates used in the IPCC projections compared to our observed VLM.
309

Table 2. Projected SLR without the contribution of vertical land motion in meters at three stations of Chesapeake Bay area including Sewell's point, Cape May, and Washington DC. Sea level projections considering projections with *medium confidence* are provided, relative to the period 1995–2014, for five Shared Socioeconomic Pathway (SSP) scenarios. The details of the scenarios can be found in the Working Group 1 contribution sections TS1.3 and 1.6 and Cross-Chapter Box 1.4 and are described as below. **SSP1-1.9** indicates net zero CO_2 emissions around the middle of the century and corresponds to warming to approximately 1.5°C above 1850-1900 in 2100 after slight overshoot (median). **SSP1-2.6** stays below 2.0°C warming relative to 1850-1900 (median) with implied net zero emissions in the second half of the century. **SSP2-4.5** is approximately in line with the upper end of aggregate Nationally Determined Contribution (NDC) emission levels by 2030. **SSP3-7.0** indicates a medium to high reference scenario resulting from no additional climate policy under the SSP3 socioeconomic development narrative. SSP3-7.0 has particularly high non-CO_2 emissions, including high aerosols emissions. **SSP5-8.5** is a high reference scenario with no additional climate policy (Source: IPCC AR6).

Tide gauge Station		***Median (50th Percentile) (m)***		
	Relative to 1995-2014	***2030***	***2050***	***2100***
Sewell's Point	SSP 1-1.9	0.138	0.260	0.458
	SSP 1-2.6	0.146	0.270	0.520
	SSP 2-4.5	0.142	0.282	0.651
	SSP 3-7.0	0.139	0.286	0.770
	SSP 5-8.5	0.148	0.312	0.862
Cape May	SSP 1-1.9	0.142	0.260	0.458

	SSP 1-2.6	0.146	0.278	0.522
	SSP 2-4.5	0.144	0.286	0.664
	SSP 3-7.0	0.141	0.286	0.784
	SSP 5-8.5	0.151	0.318	0.884
Washington D.C.	SSP 1-1.9	0.14	0.260	0.454
	SSP 1-2.6	0.145	0.275	0.520
	SSP 2-4.5	0.142	0.286	0.660
	SSP 3-7.0	0.140	0.287	0.778
	SSP 5-8.5	0.150	0.316	0.875

2.4. Strom surge estimates

We obtained recorded storm surge levels for Hurricane Isabel (Hovis et al., 2004) and Hurricane Sandy (Fanelli et al., 2013), in September 2003 and October 2012, respectively, to create indignation scenarios due to sea-level rise and storm surges, assuming that Sandy-like surges are likely to occur in the future (Lin et al., 2012). Here storm surge is defined as the local change in the elevation of the ocean along a shore due to a storm and represents the observed water level/storm tide-minus predicted astronomical tide levels, e.g., water motion which would result from Earth's rotation and gravitation effects following NOAA report (Fanelli et al., 2013; Hovis et al., 2004). Recorded details on storm surge levels, dates and time from Hurricane Sandy and Isabel used for our analysis for flood inundation can be found in Table 1. We only evaluate the effect of storm surge on inundation hazards for the high reference scenario with no additional climate policy namely SSP 5-8.5 for SLR.

339

340 ## 3. Results

341 ### 3.1. VLM rate and Validation

342 We obtained vertical land motion for 2007-2020 after processing an extensive set of
343 Sentinel-1 and ALOS SAR acquisitions and further estimated uncertainty in the rate (Fig. 4).
344 Over the Chesapeake Bay, a spatially variable subsidence rate up to -5.5 mm/year and a standard
345 deviation of maximum 1.6 mm/year is observed. A few subsidence hotspots are highlighted in
346 Figure. 4. Panels I, II, III show Southern Chesapeake Bay, Cape May, and Washington DC areas
347 where tide gauge stations are located. The southern Chesapeake Bay area, mainly the Hampton
348 region and Newport News, is undergoing subsidence with -3 ± 0.4 to -4 ± 0.4 mm/year
349 (highlighted by zoomed in panel I). To validate the InSAR-based estimate of VLM, we use a
350 subset of selected GNSS stations, comprising 20% of available stations, which were chosen
351 randomly and were not used in our analysis. We found a good agreement between the dataset,
352 with a standard deviation of 0.34 mm/yr for the difference between InSAR-based VLM and
353 GNSS vertical rate (Fig.4 panel III). Small uplift signals are observed near Calvert County,
354 Maryland, likely due to aquifer recharge, observed in the groundwater level measurement at sites
355 Prince Frederick, MD (Fig. 5A) and Cover Point, MD (Fig. 5B) from 2017 to 2021.

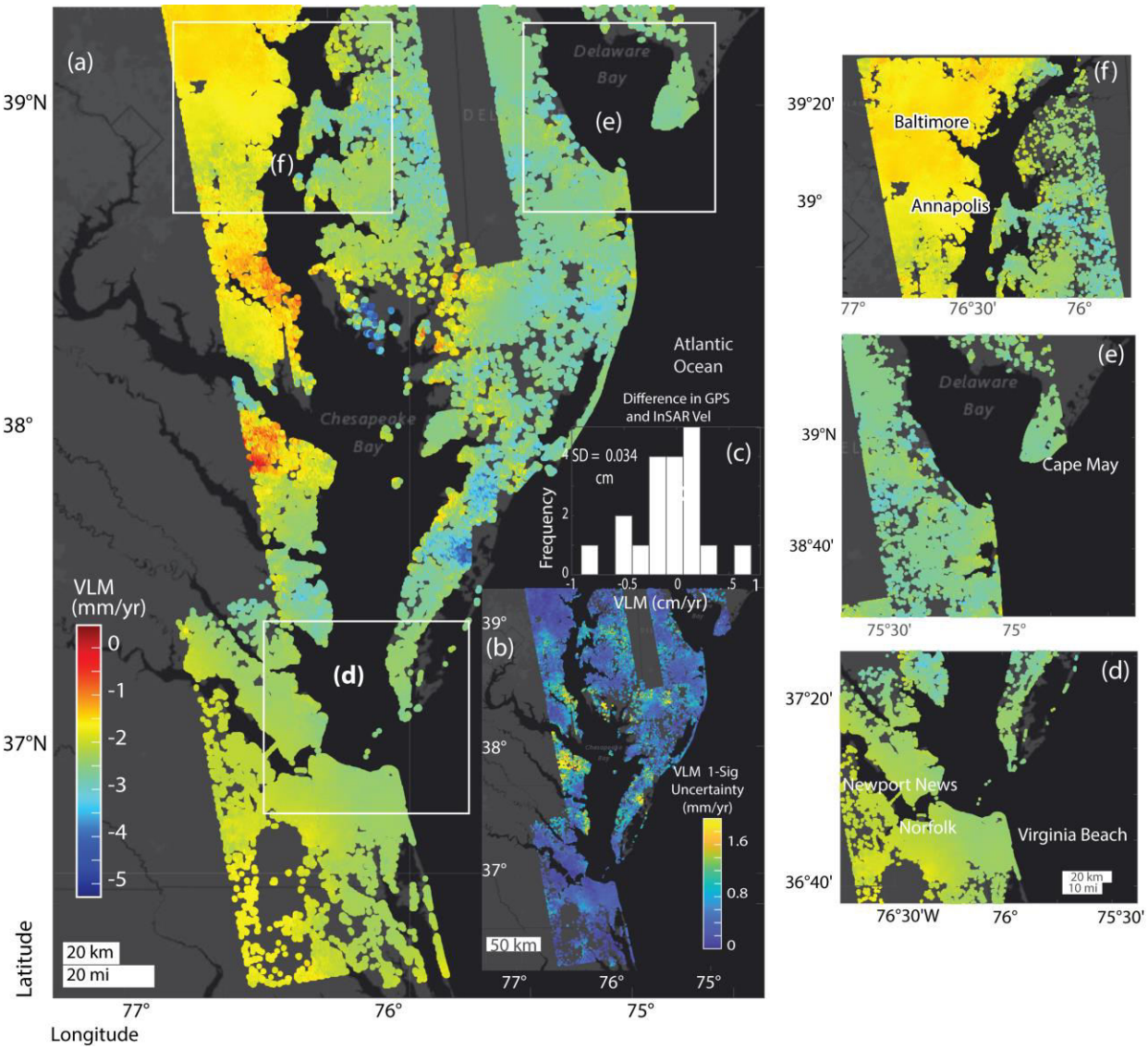

Figure.4. (a) VLM rate (mm/yr) over the Chesapeake Bay from 2007-2020 as a combination of ALOS PALSAR, Sentinel-1A and GNSS datasets. **(b)** VLM 1σ standard deviation. The validation results between the 20% GNSS station data and the estimated VLM is conducted in panel **(c)** (cm/yr). Further, boxes (d), (e), (f) show three zoomed-in locations of Chesapeake Bay, highlighted in panel (a).

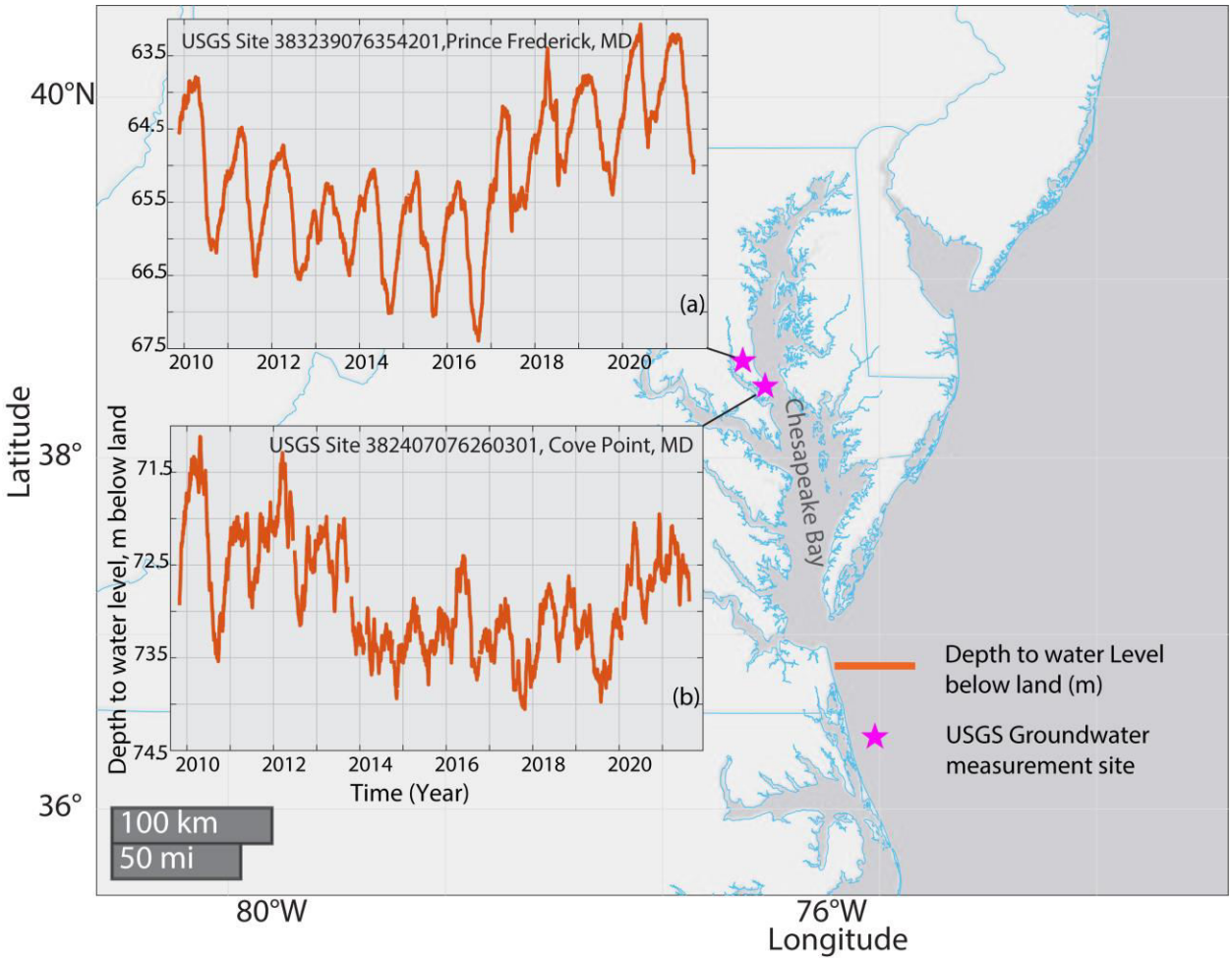

Figure 5. Timeseries of groundwater level, measured as depth to water below land at two USGS sites **(a)** Prince Frederick, MD, **(b)** Cove Point, MD.

3.2. Non-GIA Contributions

To examine the non-GIA contributions in the estimated VLM, we used the GIA ICE-6G-D model (Peltier et al., 2018) and removed its effect from the observed VLM. VLM from the GIA model projected on InSAR pixels (Fig.6A) shows a persistent collapsing forebulge of the Laurentide Ice Sheet in the study area with a median rate of -1.88 mm/yr (and range of -2.14 - -1.36 mm/yr). The InSAR-based VLM map exhibit a similar pattern but at a higher subsidence rate up to -5 mm/year, as shown in Fig. 6B (and 6A). After removing the effect of GIA (Fig. 6C

and D), the VLM rate map mainly comprises the influence of non-GIA contributions, including groundwater extraction and sediment compaction. We observe non-GIA subsidence rates as high as -4 mm/yr in some areas, 2-3 times faster than long-term geologic rates, consistent with that reported in earlier studies (e.g., Karegar et al. (2016)). After removing the GIA effect, a broader region, mainly along the coastline, shows a slow uplift rate of up to 1 mm/yr, corresponding with rebounding aquifers and possibly aggrading wetlands (Holmquist et al., 2021).

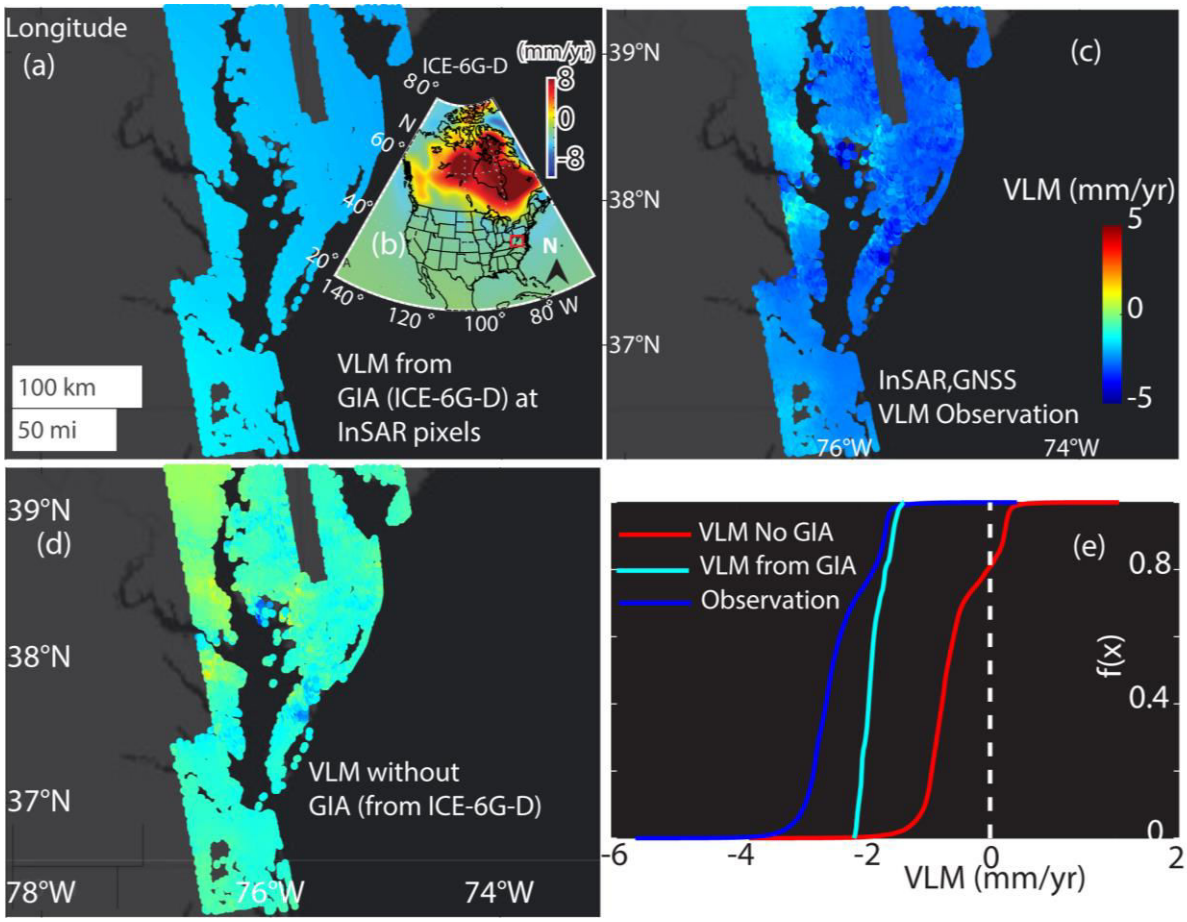

Figure 6. VLM rate with and without the influence of glacial isostatic adjustment (GIA). **(a)** VLM from GIA oversampled on InSAR pixels, data from using ICE-6G-D model (Peltier et al., 2018). **(b)** estimated VLM in this study InSAR and GNSS, and VLM. **(c)** VLM rate after removing the effect of GIA. **(d)** Empirical cumulative distribution function for datasets shown in Panels **(a), (b), (c).** Note that panels **(a), (b), (c)** have same color bar.

3.3. Comparison with IPCC VLM projections

We compared projected vertical land motion information used in IPCC Sixth Assessment Report AR6, considering its median estimates (50 percentile) with a linear projection of our VLM rates at two tide gauge stations (Fig. 7) till the 2150 time period from 2020. For vertical land motion at the tide gauge location, we selected pixels within a radius of 200 m and obtained the average rate. We found IPCC sea-level change from VLM projection was overestimated in Sewell's Point with a value of 2.85 mm/year compared to our estimate of 2.36 mm/year and underestimated in Cape May with values 2.25 mm/year versus 2.91 mm/year estimated here. This comparison highlights the need for incorporating high-resolution observation of VLM in future projections of SLR to obtain accurate estimates of future flooding and inundation hazards.

Fig. 7. Comparison of sea-level change due to vertical land motion from IPCC Sixth Assessment Report AR6, using median datasets (50 percentile) and comparison of sea-level change from our VLM estimate, at three selected tide gauge stations **(a)** Sewell's Point and **(b)** Cape May. 1-sigma error is also shown for each station. The PSMSL (Permanent Service for Mean Sea Level) ID numbers are shown based on IPCC datasets (Garner et al., 2021).

3.4. Projected Inundation Hazards

The projections of current VLM rates combined with LiDAR topographic data, SLR projection scenarios, and storm surge heights allow evaluation of future inundation hazards. These projections are required to improve preparedness and have important implications for flood mitigation and resiliency. The projected inundation areas due to only VLM in three-time snapshots, 2030, 2040, and 2100 are shown in Fig. 8, indicating increasing inundation near the wildlife reserve and coastal plains area. Inundation projections from SLR and VLM at five different climate scenarios, SSPs, from SSP 1-1.6-5-8.5 at three-time scales (2030-2050-2100) are shown in Fig. 9-13, sea-level rise inundation for 2100 time-period for all SSPs in Fig. 14 and inundated area (km^2) in Fig. 15. We observed increased inundation areas in all five SSPs 1-1.9-5-8.5 for SLR, ranging from 343, 410, 522, 587, and 627 $km^{2,}$ respectively in 2100 timeframe and 454, 483, 533, 571, and 600 from both SLR and VLM with 2100 time-period (Fig. 15, Table 3). CB's spatial inundation maps highlight areas such as Tangier island, Smith island, Mockhorn island, wetlands and National wildlife refuges such as Blackwater national wildlife refuge and Plumtree national wildlife refuge that are flooded in even very low and low GHG emissions scenarios such as SSPs 1-1.9-1-2.6 (Fig. 9 and Fig. 10). The flooded area starts extending toward mostly river channels as the climate scenarios and projection time-period increase. Further, the flooded area grows toward mostly river channels as the climate scenarios and projection time-period increase.

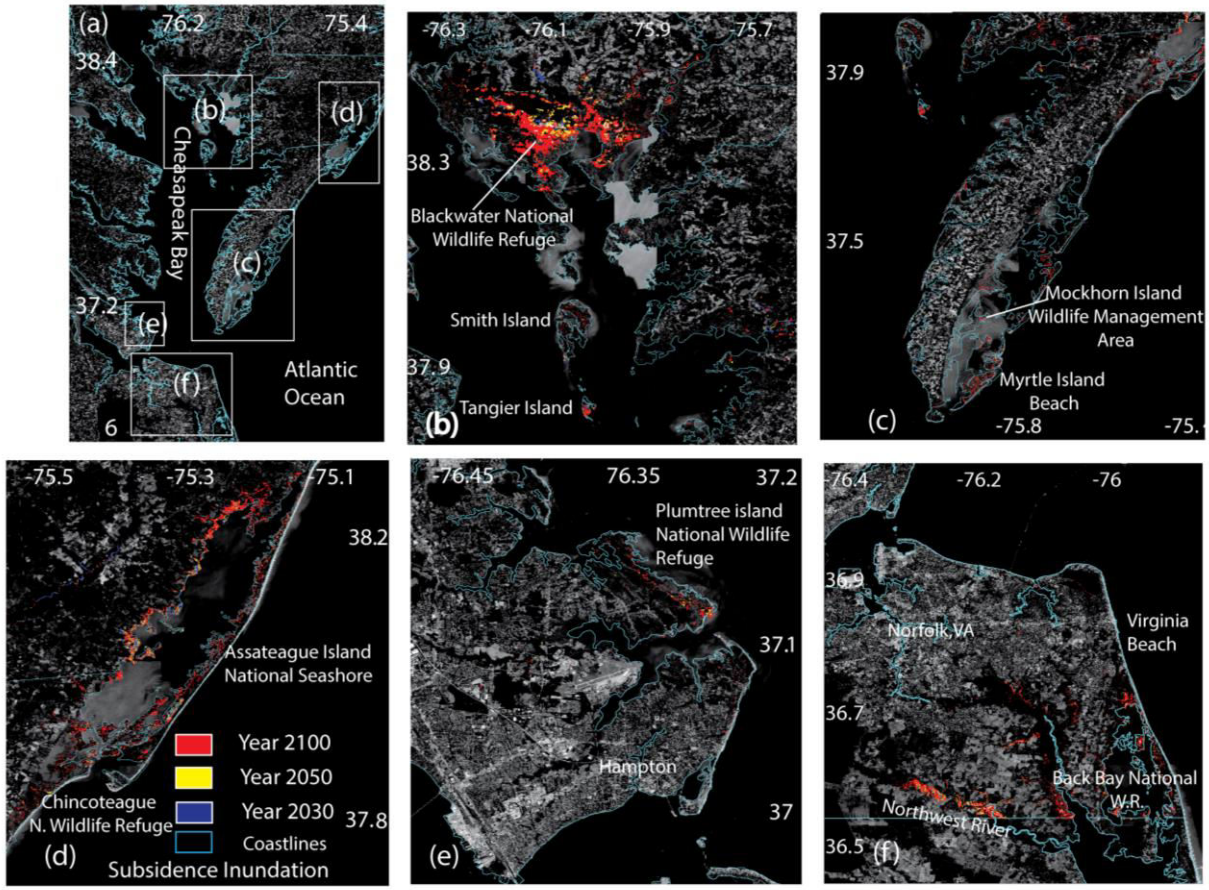

424

425 **Figure 8.** Projected inundation area from subsidence at year 2030, 2050, and 2100 using our VLM
426 measurement. Panel **(a)** shows the overview and panels **(b), (c), (d), (e), (f)** highlights the zoomed-in
427 subsidence inundation for three timescales.

428

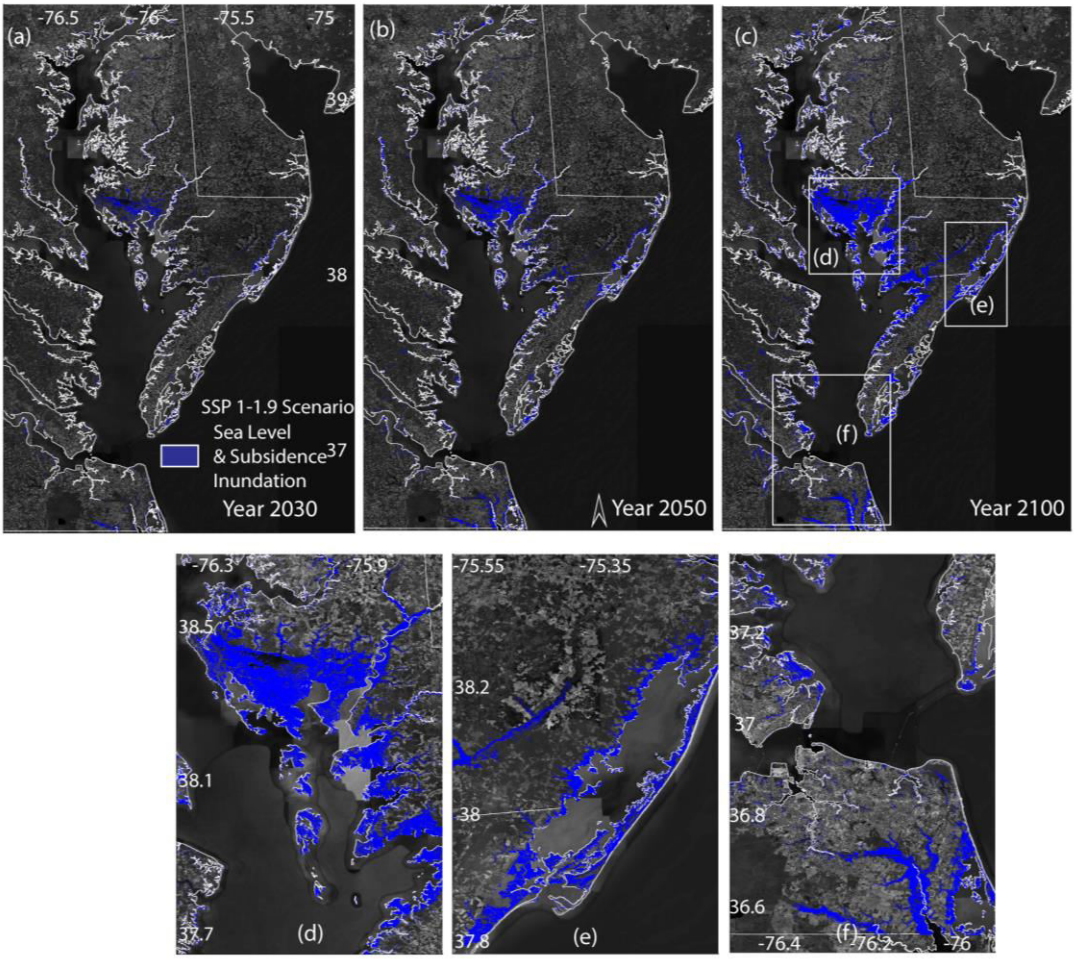

Figure 9. Projected Inundation area from both subsidence and SLR under Shared Socioeconomic Pathways (SSP) 1-1.9 at year 2030, 2050, and 2100 (top panels, panels **(a), (b), (c)** respectively). The bottom panel **(d), (e), (f)** highlights zoomed-in inundation from sea level and subsidence at 2100.

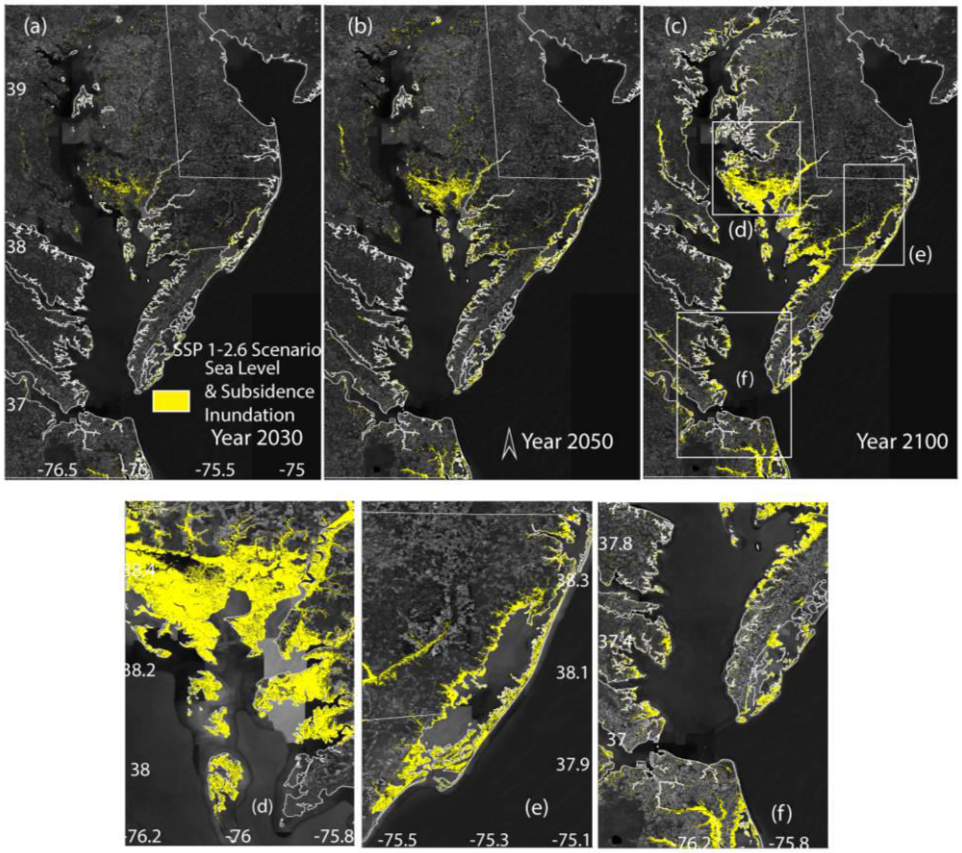

435

436 **Figure 10.** Projected inundation area both subsidence and SLR at Shared Socioeconomic Pathways (SSP)

437 1-2.6 for timescales 2030, 2050, and 2100 (top panels, panels **(a), (b), (c)** respectively). The bottom

438 panels, **(d), (e), (f)** highlights zoomed-in inundation from sea level and subsidence at 2100.

439

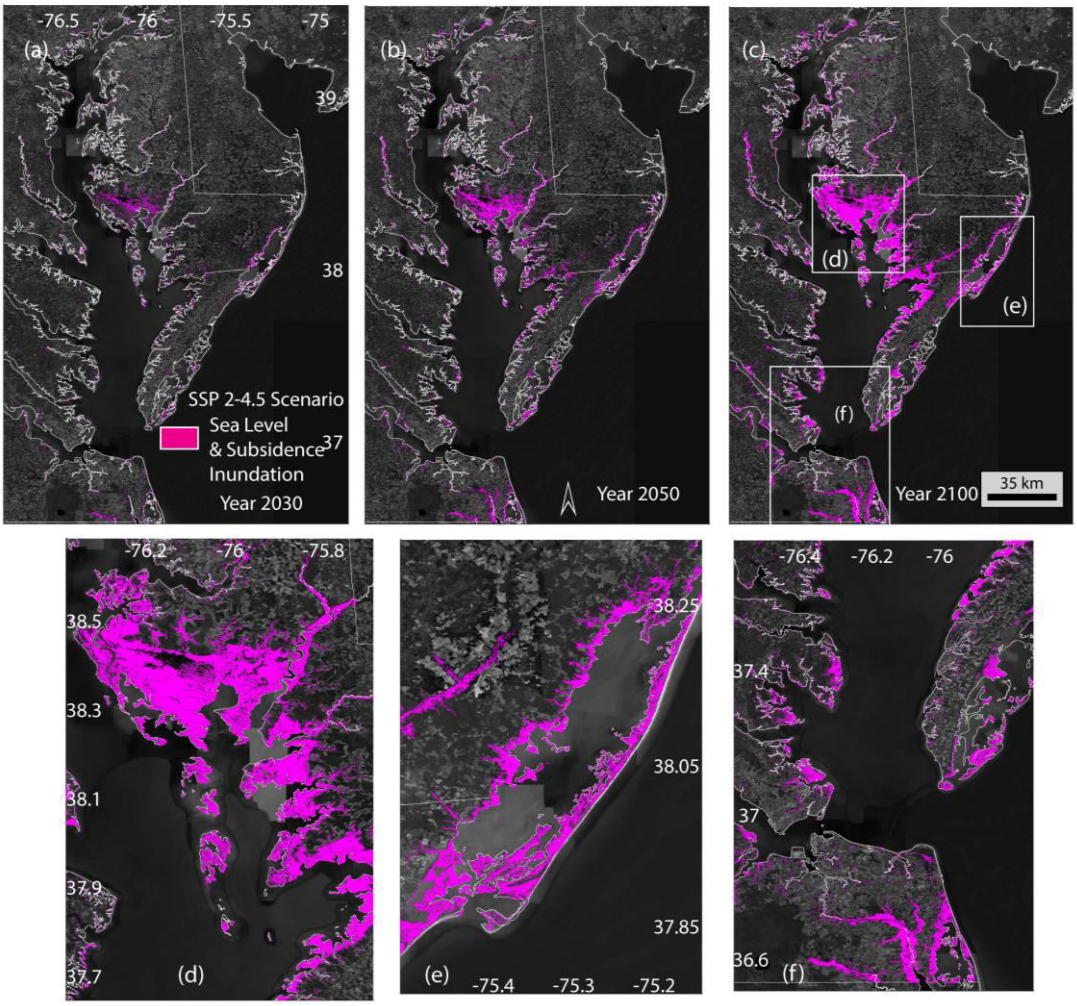

440

441 **Figure 11**. Projected inundation area from both subsidence and SLR at Shared Socioeconomic Pathways

442 (SSP) 2-4.5 for timescales 2030, 2050, and 2100 (top panels, panels **(a), (b), (c)** respectively). The bottom

443 panels **(d), (e), (f)** highlights zoomed-in inundation from sea level and subsidence at 2100.

444

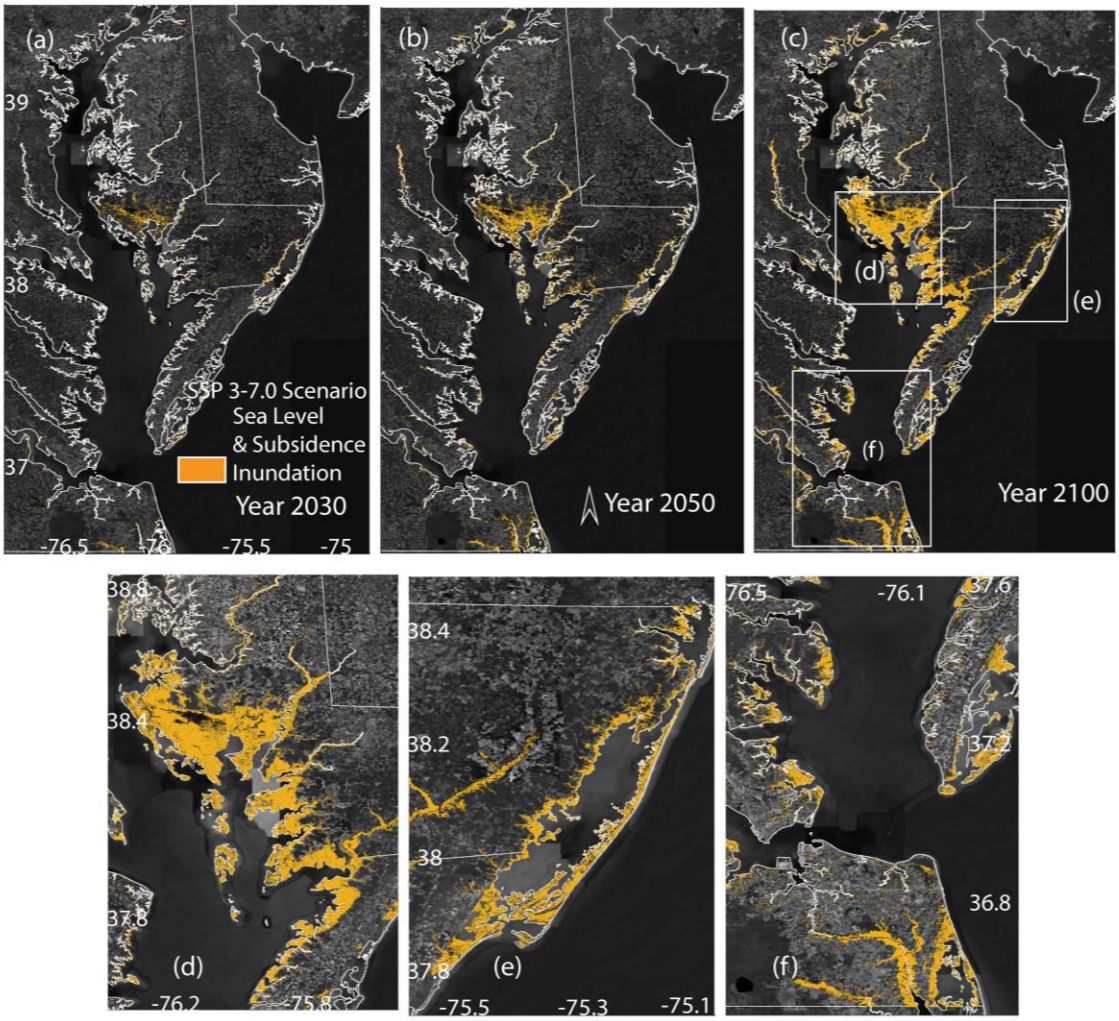

445

446 **Fig.12.** Projected inundation area from both subsidence and SLR at Shared Socioeconomic Pathways

447 (SSP) 3-7.0 for timescales 2030, 2050, and 2100 (top panels, panels **(a), (b), (c)** respectively). The bottom

448 panel **(d), (e), (f)** highlights zoomed-in inundation from sea level and subsidence at 2100.

449

450

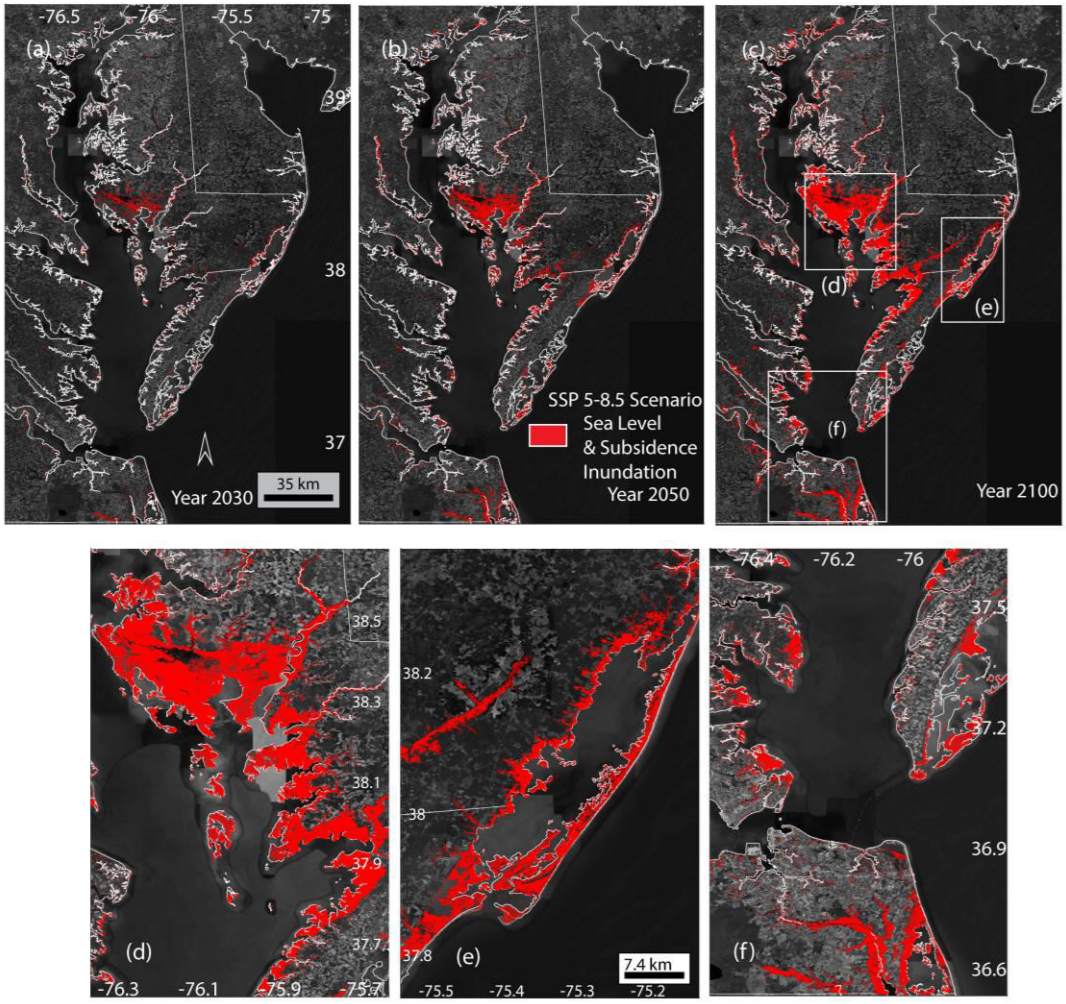

451

452 **Figure 13.** Projected inundation area from both subsidence and SLR at Shared Socioeconomic Pathways
453 (SSP) 5-8.5 for timescales 2030, 2050, and 2100 (top panels, panels **(a), (b), (c)** respectively). Bottom
454 panel **(d), (e), (f)** highlights zoomed-in inundation from sea level and subsidence in 2100.

455

456

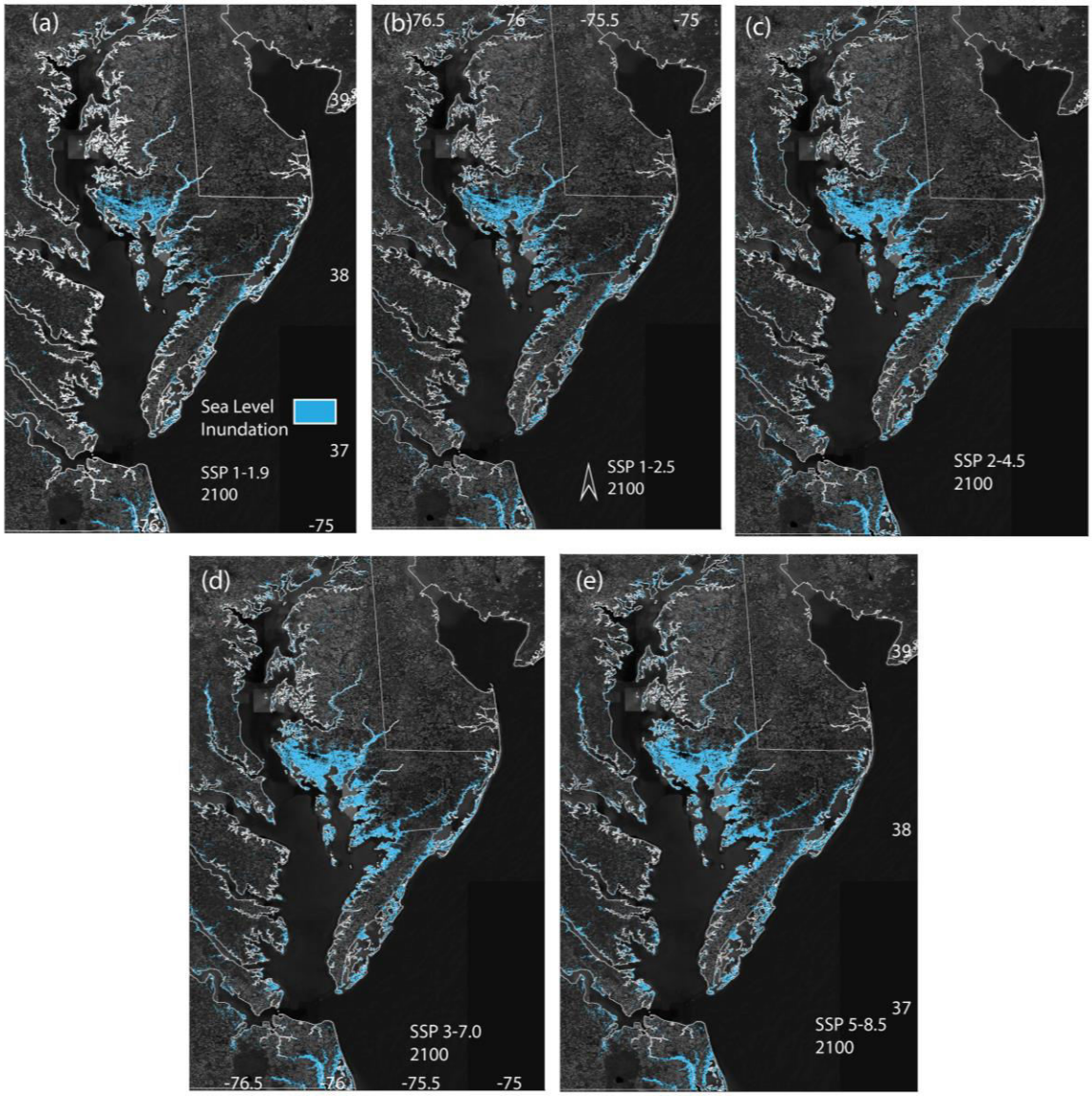

457

458 **Figure 14.** Projected inundation area from SLR for time 2100 all SSPs, 1-1.9, 1-2.5, 2-4.5, top panels **(a),**
459 **(b), (c)**, bottom panels **(d), (e) are** 3-7.0, and 5-8.5 respectively for the Chesapeake Bay.

460

461 At SSP 3-7.0 and 5-8.5 in 2100 time-period, we observed more inundation from only sea-
462 level rise ranging from 587 and 627 km^2 in contrast to while including VLM effect in the
463 projection resulting in 571 and 600 km^2 showing the result of non-linear VLM and role of uplift

pixels in the overall inundation area (Fig. 15, Table 3). The combination of the storm surge scenario from Hurricane Sandy in October 2012, with the SLR showed an inundated area of 578-1087 km^2, respectively, from 2030 to 2100 (Fig.16A) in SSP 5-8.5 and 599-1232 km^2 when incorporating Hurricane Isabel of September 2003 (Fig. 16B). Further, an amalgamation of all three components SLR, VLM, and Strom surge, projected inundation of 739-1032 km^2 and 588-1117 km^2 for Hurricane Sandy and Isabel, respectively.

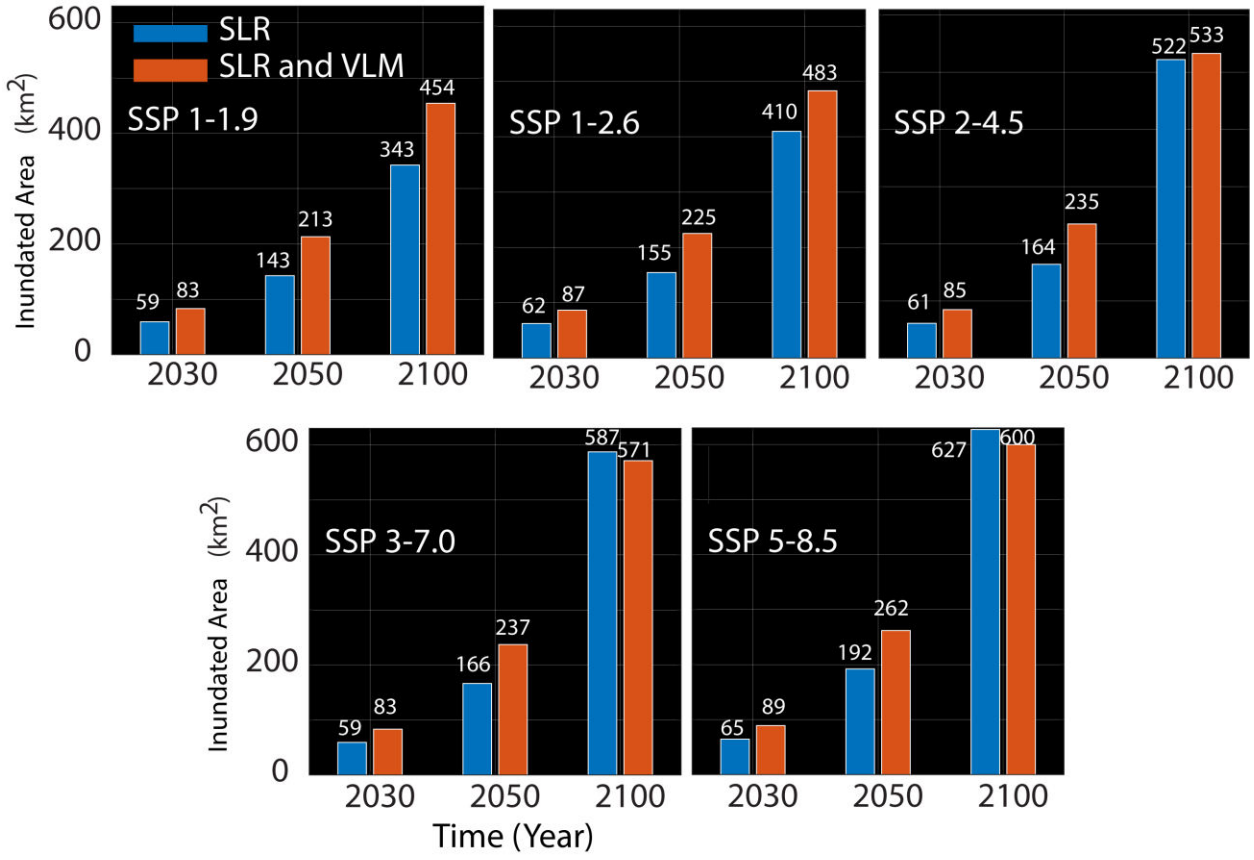

Fig. 15. Inundated Area from Subsidence and SLR (km^2) (in orange), and only SLR (in blue in km^2) at SSPs 1-1.9, 1-2.5, 2-4.5, 3-7.0, and 5-8.5 respectively.

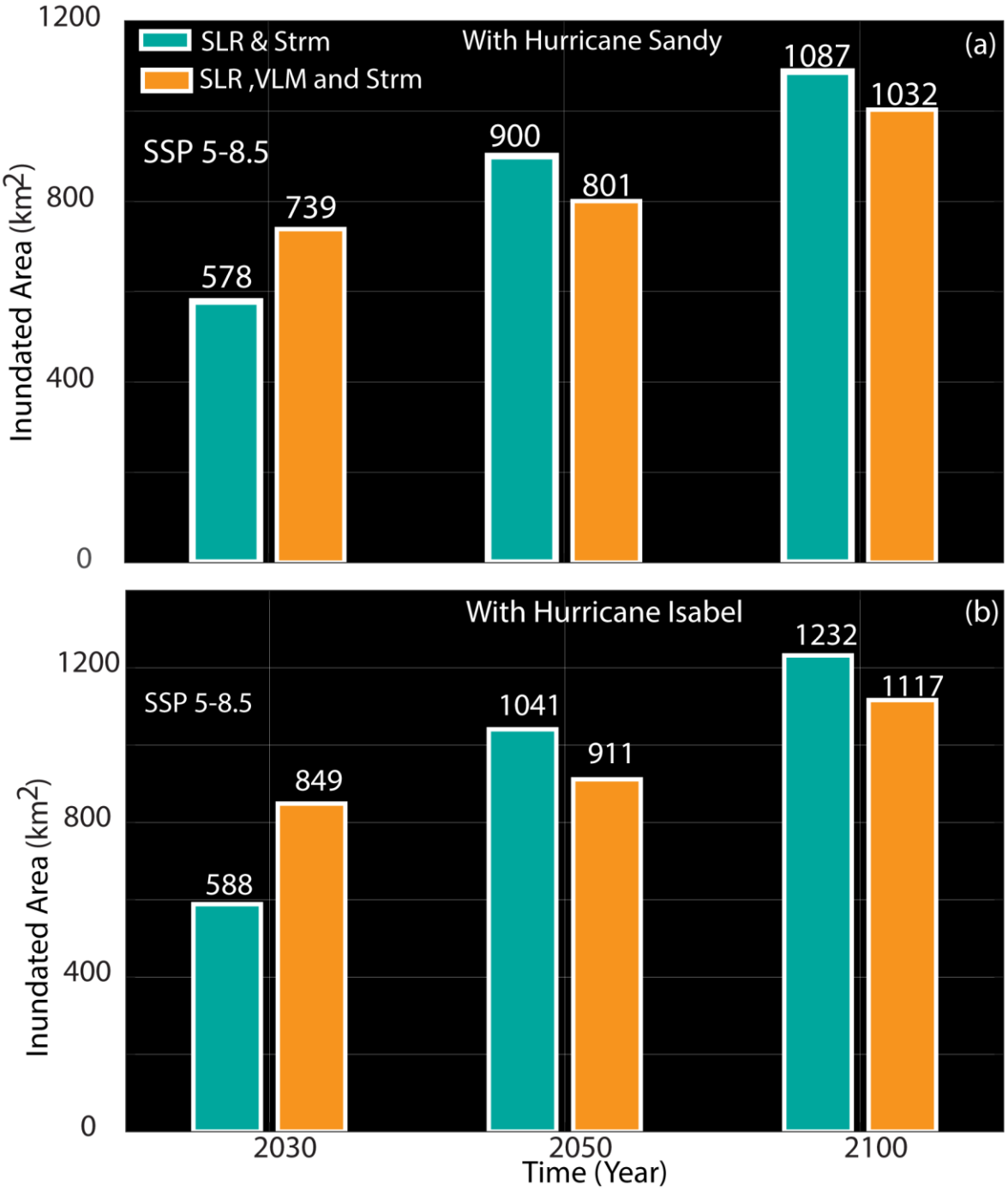

Fig.16. Inundation Area (km^2) from Storm surge based on **(a)** October 2012 Hurricane Sandy Datasets and **(b)** Hurricane Isabel recorded on 18-19 September 2003 from NOAA and SLR scenario of highest emission SSP 5-8.5 in km^2.

Table 3. Inundated area (km^2) modeled for five climate scenarios for Sea-Level Rise (SLR), Sea Level Rise and Subsidence from 2030 through 2100 and SLR, storm surge and VLM incorporating Hurricane Sandy of October 2012 and Hurricane Isabel of September 2003, for high reference scenario with no additional climate policy, SSP 5-8.5 from 2030 to 2100.

Content		***Year***		
		2030	***2050***	***2100***
	IPCC Climate Scenarios	***Area (Km^2)***	***Area (Km^2)***	***Area (Km^2)***
Sea Level Rise	SSP 1-1.9	59	143	342
	SSP 1-2.6	62	155	410
	SSP 2-4.5	61	164	522
	SSP 3-7.0	59	166	587
	SSP 5-8.5	65	192	627
Sea Level Rise and Subsidence	SSP 1-1.9	83	213	454
	SSP 1-2.6	87	225	483
	SSP 2-4.5	85	235	533
	SSP 3-7.0	83	237	571
	SSP 5-8.5	89	262	600
Sea Level Rise and Storm Surge (Hurricane Sandy)	SSP 5-8.5	578	900	1087
Sea Level Rise, Storm	SSP 5-8.5	739	801	1032

Surge, and VLM (*Hurricane Sandy*)				
Sea Level Rise and Storm Surge (Hurricane Isabel)	SSP 5-8.5	588	1041	1232
Sea Level Rise, Storm Surge, and VLM (*Hurricane Isabel*)	SSP 5-8.5	849	911	1117

4. Discussion and Conclusion

The Chesapeake Bay area, the largest estuary in the United States, is home to 15 wildlife refuges (Ernst, 2003; Ray & McCormick-Ray, 2009). The urban Hampton area encompasses the world's most extensive naval base and a dense population of more than 1.7 million people (U.S. Census Bureau, 2020). Accurate estimation of VLM and flooding coming from sea level change allows flood mitigation. A recent study on the region has highlighted increasing regional sea-level changes in the Chesapeake Bay area (Bekaert et al., 2017; Buzzanga et al., 2020; Harvey et al., 2021; Karegar et al., 2017). Here we provide accurate high-resolution observations and estimate changes in local processes driving relative sea-level change and inundation projection until 2100, encompassing factors contributing to sea level.

Combining ALOS and Sentinel-1 datasets with GNSS measurements allows obtaining robust estimates of long-term VLM at management-relevant resolution (10s m) for the period 2007-2020, suitable for investigating natural and anthropogenic drivers and relative sea-level rise and inundation hazards. To perform our analysis, we assumed that the VLM rates were steady during

the observation period and we ignored the gap from 2011 to 2014 between the two satellite acquisition periods. Thus, a decadal change in VLM rates may affect the estimated long-term trends. However, a comparison with independent GNSS measurements yields a good agreement, suggesting our assumptions are reasonable and decadal VLM rate variations are of 2nd order importance. Forward projections of VLM are crucial for assessing future flooding and inundation hazards. Following earlier studies (Fox-Kemper et al., 2021; Miller & Shirzaei, 2021; Manoochehr Shirzaei & Bürgmann, 2018), we assumed a linear functional model for future estimates. However, this assumption might only be valid for the GIA effect, and most anthropogenic factors, such as contributions from aquifer compaction, are likely non-linear and change over time (Manoochehr Shirzaei et al., 2021). The Chesapeake Bay region, particularly Hampton Roads, injects treated wastewater into the underlying aquifer to mitigate subsidence from aquifer compaction. A recent study by Buzzanga et al. (2020) on Hampton reported an overall subsidence rate of -3.6 ± 2.3 mm/year with considerable spatial variability and no significant effects of groundwater injection. Despite its importance, thus far little research has focused on scenario-based projections of coastal VLM that account for various socioeconomic and climate forcing factors to obtain values comparable to that of SLR projections.

Using a VLM-adjusted high resolution (1x1 m grid) lidar topographic dataset alongside IPCC AR6 sea level scenario and two Hurricanes, Sandy and Isabel, allowed estimation of flood and inundation extent in the Chesapeake Bay throughout 21st century. Overall, subsidence increases the hazards, except at a few locations, where some uplift is observed due to aquifer recharge and wetlands elevation gains. These results highlight the disruptive role of VLM in defending against and adapting to climate change in coastal areas.

In the United States, almost 29% of the US population live along the coastline, with more than 41 million people living on the Atlantic coast, including a minority population, and are vulnerable to hurricanes alongside an increase in sea level (US Census Bureau, 2021). A study by Neumann et al. (2015) has projected the global coastal population to surpass one billion people this century. Flooding and inundation hazards can displace a large proportion of the population (Hauer et al., 2020). This further influences human migration due to permanent, irreversible inundation of low-elevation areas, which, under SLR, renders unavailable for livelihoods and ultimately land uninhabitable (Hauer et al., 2020). In Hampton Roads, flooding impacts low-income, socially vulnerable areas such as portions of Newport News, Norfolk, and Portsmouth, and some outlying rural areas in the counties of Gloucester and Surry. The most recent Census data lists the City of Norfolk as having 19.7% of its population living in poverty, Portsmouth as having 17.2%, and Newport News as having 15.5% (U.S. Census Bureau, 2021) and an increase in future flooding risk will disproportionately impact Black communities while remaining concentrated on the Atlantic and Gulf coasts. Our findings of current and future coastal hazards in the Chesapeake Bay, driven by climate and solid Earth changes, provide critical information for hazard and risk management and have a significant societal relevance as they induce considerable adaptation needs for disaster resilience.

Acknowledgments

The work of Sonam Futi Sherpa was supported by NASA Grant 80NSSC170567 and in part by the National Science Foundation under Grant Number 1735139. Any opinions, findings, and conclusions or recommendations expressed in this material are those of the authors and do not necessarily reflect the views of the National Science Foundation. Manoochehr Shirzaei is

supported by NASA Grant 80NSSC170567. The support of Geological Society of America (GSA) is acknowledged here. We thank the projection authors for developing and making the sea-level rise projections available, multiple funding agencies for supporting the development of the projections, and the NASA Sea-Level Change Team for developing and hosting the IPCC AR6 Sea-Level Projection Tool.

Data Availability Statement

SAR datasets are available at the Alaska satellite facilities https://vertex.daac.asf.alaska.edu/. GNSS velocities information is obtained from the Nevada Geodetic lab (http://geodesy.unr.edu/). Tide gauge datasets are found on the NOAA website https://tidesandcurrents.noaa.gov/map/index.html. The LiDAR dataset is a contribution from USGS and can be found at https://coast.noaa.gov/htdata/raster2/elevation/Chesapeake_Coned_update_DEM_2016_8656/.

References

Allen, M. J., & Allen, T. R. (2019). Precipitation Trends across the Commonwealth of Virginia (1947–2016). *Virginia Journal of Science*, *70*(1), 4.

Bekaert, D. P. S., Hamlington, B. D., Buzzanga, B., & Jones, C. E. (2017). Spaceborne Synthetic Aperture Radar Survey of Subsidence in Hampton Roads, Virginia (USA). *Scientific Reports*, *7*(1), 14752. https://doi.org/10.1038/s41598-017-15309-5

Blackwell, E., Shirzaei, M., Ojha, C., & Werth, S. (2020). Tracking California's sinking coast from space: Implications for relative sea-level rise. *Science Advances*. https://doi.org/10.1126/sciadv.aba4551

570 Blake, E. S., Kimberlain, T. B., Berg, R. J., Cangialosi, J. P., & Beven, J. L. (2013). *Tropical*
571 *cyclone report hurricane Sandy (AL182012) 22–29 October 2012. National Hurricane*
572 *Center*.
573 Blewitt, G., Hammond, W. C., & Kreemer, C. (2018). Harnessing the GPS data explosion for
574 interdisciplinary science. *Eos*, *99*(10.1029), 485.
575 Boon, J., Brubaker, J., & Forrest, D. (2010). Chesapeake Bay Land Subsidence and Sea Level
576 Change : an evaluation of past and present trends and future outlook. *Reports*.
577 https://doi.org/10.21220/V58X4P
578 Boon, J. D. (2018). Anthropocene Sea Level Change: A History of Recent Trends Observed in
579 the U.S. East, Gulf, and West Coast Regions. https://doi.org/10.21220/V5T17T
580 Bureau, U. C. (n.d.). Emergency Management Coastal Areas. Retrieved February 8, 2022, from
581 https://www.census.gov/topics/preparedness/about/coastal-areas.html
582 Bürgmann, R., Rosen, P. A., & Fielding, E. J. (2000). Synthetic Aperture Radar Interferometry
583 to Measure Earth's Surface Topography and Its Deformation. *Annual Review of Earth*
584 *and Planetary Sciences*, *28*(1), 169–209. https://doi.org/10.1146/annurev.earth.28.1.169
585 Buzzanga, B., Bekaert, D. P. S., Hamlington, B. D., & Sangha, S. S. (2020). Toward Sustained
586 Monitoring of Subsidence at the Coast Using InSAR and GPS: An Application in
587 Hampton Roads, Virginia. *Geophysical Research Letters*, *47*(18), e2020GL090013.
588 https://doi.org/10.1029/2020GL090013
589 Cho, K.-H., Wang, H. V., Shen, J., Valle-Levinson, A., & Teng, Y. (2012). A modeling study on
590 the response of Chesapeake Bay to hurricane events of Floyd and Isabel. *Ocean*
591 *Modelling*, *49–50*, 22–46. https://doi.org/10.1016/j.ocemod.2012.02.005

592 Costantini, M. (1998). A novel phase unwrapping method based on network programming. *IEEE*
593 *Transactions on Geoscience and Remote Sensing*, *36*(3), 813–821.
594 https://doi.org/10.1109/36.673674
595 Costantini, M., & Rosen, P. A. (1999). A generalized phase unwrapping approach for sparse
596 data. In *IEEE 1999 International Geoscience and Remote Sensing Symposium.*
597 *IGARSS'99 (Cat. No.99CH36293)* (Vol. 1, pp. 267–269 vol.1).
598 https://doi.org/10.1109/IGARSS.1999.773467
599 Dangendorf, S., Hay, C., Calafat, F. M., Marcos, M., Piecuch, C. G., Berk, K., & Jensen, J.
600 (2019). Persistent acceleration in global sea-level rise since the 1960s. *Nature Climate*
601 *Change*, *9*(9), 705–710. https://doi.org/10.1038/s41558-019-0531-8
602 Davis, J. L., & Vinogradova, N. T. (2017). Causes of accelerating sea level on the East Coast of
603 North America. *Geophysical Research Letters*, *44*(10), 5133–5141.
604 https://doi.org/10.1002/2017GL072845
605 Eggleston, J., & Pope, J. (2013). *Land Subsidence and Relative Sea-Level Rise in the Southern*
606 *Chesapeake Bay Region* (Circular No. 1392). U.S. Geological Survey.
607 Ernst, H. R. (2003). *Chesapeake Bay blues: Science, politics, and the struggle to save the bay*.
608 Rowman & Littlefield.
609 Ezer, T., & Corlett, W. B. (2012). Is sea level rise accelerating in the Chesapeake Bay? A
610 demonstration of a novel new approach for analyzing sea level data. *Geophysical*
611 *Research Letters*, *39*(19). https://doi.org/10.1029/2012GL053435
612 Fanelli, C., Fanelli, P., & Wolcott, D. (2013). *Hurricane Sandy* (NOAA Water Level and
613 Meteorological Data Report). National Oceanic and Atmospheric Administration, US
614 Department of Commerce. Retrieved from

https://tidesandcurrents.noaa.gov/publications/Hurricane_Sandy_2012_Water_Level_and_Meteorological_Data_Report.pdf

Fox-Kemper, B., Hewitt, H. T., Aðalgeirsdóttir, G., Drijfhout, S. S., Edwards, T. L., Golledge, N. R., et al. (2021). *Ocean, Cryosphere and Sea Level Change. In Climate Change 2021: The Physical Science Basis. Contribution of Working Group I to the Sixth Assessment Report of the Intergovernmental Panel on Climate Change e [MassonDelmotte, V., P. Zhai, A. Pirani, S.L. Connors, C. Péan, S. Berger, N. Caud, Y. Chen, L. Goldfarb, M.I. Gomis, M. Huang, K. Leitzell, E. Lonnoy, J.B.R. Matthews, T.K. Maycock, T. Waterfield, O. Yelekçi, R. Yu, and B. Zhou (eds.)]. Cambridge University Press. In Press.*

Franceschetti, G., & Lanari, R. (1999). Synthetic aperture radar processing CRC press. *Electronic Engineering Systems Series*.

Frederikse, T., Landerer, F., Caron, L., Adhikari, S., Parkes, D., Humphrey, V. W., et al. (2020). The causes of sea-level rise since 1900. *Nature*, *584*(7821), 393–397. https://doi.org/10.1038/s41586-020-2591-3

Garner, G. G., Hermans, T., Kopp, R. E., Slangen, A. B. A., Edwards, T. L., Levermann, S., et al. (2021). *IPCC AR6 Sea-Level Rise Projections. Version 20210809. PO.DAAC, CA, USA.*

Garner, G. G., Kopp, R. E., Hermans, T., Slangen, A. B. A., Koubbe, M., Turilli, M., et al. (In prep). *Framework for Assessing Changes To Sea-level (FACTS). Geoscientific Model Development.*

Gill, S. K., & Schultz, J. R. (2001). *Tidal datums and their applications.* (Report). NOAA, NOS Center for Operational Oceanographic Products and Services. https://doi.org/10.25607/OBP-170

638 Hammond, W. C., Blewitt, G., & Kreemer, C. (2016). GPS Imaging of vertical land motion in
639 California and Nevada: Implications for Sierra Nevada uplift. *Journal of Geophysical*
640 *Research: Solid Earth*, *121*(10), 7681–7703. https://doi.org/10.1002/2016JB013458
641 Hanssen, R. F. (2001). *Radar interferometry: data interpretation and error analysis* (Vol. 2).
642 Springer Science & Business Media.
643 Harvey, T. C., Hamlington, B. D., Frederikse, T., Nerem, R. S., Piecuch, C. G., Hammond, W.
644 C., et al. (2021). Ocean mass, sterodynamic effects, and vertical land motion largely
645 explain US coast relative sea level rise. *Communications Earth & Environment*, *2*(1), 1–
646 10. https://doi.org/10.1038/s43247-021-00300-w
647 Hauer, M. E., Fussell, E., Mueller, V., Burkett, M., Call, M., Abel, K., et al. (2020). Sea-level
648 rise and human migration. *Nature Reviews Earth & Environment*, *1*(1), 28–39.
649 https://doi.org/10.1038/s43017-019-0002-9
650 Holmquist, J. R., Brown, L. N., & MacDonald, G. M. (2021). Localized Scenarios and
651 Latitudinal Patterns of Vertical and Lateral Resilience of Tidal Marshes to Sea-Level
652 Rise in the Contiguous United States. *Earth's Future*, *9*(6), e2020EF001804.
653 https://doi.org/10.1029/2020EF001804
654 Homer, C. G., Fry, J. A., & Barnes, C. A. (2012). *The National Land Cover Database* (No.
655 2012–3020). *Fact Sheet*. U.S. Geological Survey. https://doi.org/10.3133/fs20123020
656 Hovis, J., Popovich, W., Zervas, C., Hubbard, J., Shih, H. H., & Stone, P. (2004). *Effects of*
657 *Hurricane Isable on Water Levels Data Report* (Technical Report) (p. 120). National
658 Oceanic and Atmospheric Administration, US Department of Commerce. Retrieved from
659 https://tidesandcurrents.noaa.gov/publications/techrpt40.pdf

IPCC. (2021): *Climate Change 2021: The Physical Science Basis. Contribution of Working Group I to the Sixth Assessment Report of the Intergovernmental Panel on Climate Change [Masson-Delmotte, V., P. Zhai, A. Pirani, S.L. Connors, C. Péan, S. Berger, N. Caud, Y. Chen, L. Goldfarb, M.I. Gomis, M. Huang, K. Leitzell, E. Lonnoy, J.B.R. Matthews, T.K. Maycock, T. Waterfield, O. Yelekçi, R. Yu, and B. Zhou (eds.)]. Cambridge University Press. In Press*.

IPCC. (2021): *Summary for Policymakers. In: Climate Change 2021: The Physical Science Basis. Contribution of Working Group I to the Sixth Assessment Report of the Intergovernmental Panel on Climate Change [MassonDelmotte, V., P. Zhai, A. Pirani, S.L. Connors, C. Péan, S. Berger, N. Caud, Y. Chen, L. Goldfarb, M.I. Gomis, M. Huang, K. Leitzell, E. Lonnoy, J.B.R. Matthews, T.K. Maycock, T. Waterfield, O. Yelekçi, R. Yu, and B. Zhou (eds.)]. Cambridge University Press. In Press.*

Karegar, M. A., Dixon, T. H., & Engelhart, S. E. (2016). Subsidence along the Atlantic Coast of North America: Insights from GPS and late Holocene relative sea level data. *Geophysical Research Letters*, *43*(7), 3126–3133. https://doi.org/10.1002/2016GL068015

Karegar, M. A., Dixon, T. H., Malservisi, R., Kusche, J., & Engelhart, S. E. (2017). Nuisance Flooding and Relative Sea-Level Rise: the Importance of Present-Day Land Motion. *Scientific Reports*, *7*(1), 11197. https://doi.org/10.1038/s41598-017-11544-y

Lin, N., Emanuel, K., Oppenheimer, M., & Vanmarcke, E. (2012). Physically based assessment of hurricane surge threat under climate change. *Nature Climate Change*, *2*(6), 462–467. https://doi.org/10.1038/nclimate1389

McFarland, R. E., & Scott, B. T. (2006). *The Virginia coastal plain hydrogeologic framework*.

682 Miller, M. M., & Shirzaei, M. (2021). Assessment of future flood hazards for southeastern
683 Texas: Synthesizing subsidence, sea-level rise, and storm surge scenarios. *Geophysical*
684 *Research Letters*, *48*(8), e2021GL092544.
685 Nerem, R. S., Beckley, B. D., Fasullo, J. T., Hamlington, B. D., Masters, D., & Mitchum, G. T.
686 (2018). Climate-change–driven accelerated sea-level rise detected in the altimeter era.
687 *Proceedings of the National Academy of Sciences*, *115*(9), 2022–2025.
688 https://doi.org/10.1073/pnas.1717312115
689 Neumann, B., Vafeidis, A. T., Zimmermann, J., & Nicholls, R. J. (2015). Future Coastal
690 Population Growth and Exposure to Sea-Level Rise and Coastal Flooding - A Global
691 Assessment. *PLOS ONE*, *10*(3), e0118571. https://doi.org/10.1371/journal.pone.0118571
692 OCM Partners. (2021). 2016 USGS CoNED Topobathymetric Model (1859 - 2015): Chesapeake
693 Bay Region from 2010-06-15 to 2010-08-15. NOAA National Centers for Environmental
694 Information. Retrieved from https://www.fisheries.noaa.gov/inport/item/55321.
695 Ojha, C., Shirzaei, M., Werth, S., Argus, D. F., & Farr, T. G. (2018). Sustained groundwater loss
696 in California's Central Valley exacerbated by intense drought periods. *Water Resources*
697 *Research*, *54*(7), 4449–4460.
698 O'Neill, B. C., Kriegler, E., Riahi, K., Ebi, K. L., Hallegatte, S., Carter, T. R., et al. (2014). A
699 new scenario framework for climate change research: the concept of shared
700 socioeconomic pathways. *Climatic Change*, *122*(3), 387–400.
701 https://doi.org/10.1007/s10584-013-0905-2
702 Peltier, W. R., Argus, D. F., & Drummond, R. (2018). Comment on "An Assessment of the ICE-
703 6G_C (VM5a) Glacial Isostatic Adjustment Model" by Purcell et al. *Journal of*

Geophysical Research: Solid Earth, *123*(2), 2019–2028. https://doi.org/10.1002/2016JB013844

Ray, G. C., & McCormick-Ray, J. (2009). *Coastal-marine conservation: science and policy*. John Wiley & Sons.

Riahi, K., van Vuuren, D. P., Kriegler, E., Edmonds, J., O'Neill, B. C., Fujimori, S., et al. (2017). The Shared Socioeconomic Pathways and their energy, land use, and greenhouse gas emissions implications: An overview. *Global Environmental Change*, *42*, 153–168. https://doi.org/10.1016/j.gloenvcha.2016.05.009

Sallenger, A. H., Doran, K. S., & Howd, P. A. (2012). Hotspot of accelerated sea-level rise on the Atlantic coast of North America. *Nature Climate Change*, *2*(12), 884–888. https://doi.org/10.1038/nclimate1597

Sella, G. F., Stein, S., Dixon, T. H., Craymer, M., James, T. S., Mazzotti, S., & Dokka, R. K. (2007). Observation of glacial isostatic adjustment in "stable" North America with GPS. *Geophysical Research Letters*, *34*(2). https://doi.org/10.1029/2006GL027081

Shen, J., Wang, H., Sisson, M., & Gong, W. (2006). Storm tide simulation in the Chesapeake Bay using an unstructured grid model. *Estuarine, Coastal and Shelf Science*, *68*(1), 1–16. https://doi.org/10.1016/j.ecss.2005.12.018

Sheng, Y. P., Alymov, V., & Paramygin, V. A. (2010). Simulation of storm surge, wave, currents, and inundation in the Outer Banks and Chesapeake Bay during Hurricane Isabel in 2003: The importance of waves. *Journal of Geophysical Research: Oceans*, *115*(C4).

Shirzaei, M. (2013). A Wavelet-Based Multitemporal DInSAR Algorithm for Monitoring Ground Surface Motion. *IEEE Geoscience and Remote Sensing Letters*, *10*(3), 456–460. https://doi.org/10.1109/LGRS.2012.2208935

727 Shirzaei, M., & Bürgmann, R. (2012). Topography correlated atmospheric delay correction in
728 radar interferometry using wavelet transforms. *Geophysical Research Letters*, *39*(1).
729 https://doi.org/10.1029/2011GL049971
730 Shirzaei, Manoochehr, & Bürgmann, R. (2018). Global climate change and local land subsidence
731 exacerbate inundation risk to the San Francisco Bay Area. *Science Advances*, *4*(3),
732 eaap9234. https://doi.org/10.1126/sciadv.aap9234
733 Shirzaei, Manoochehr, & Walter, T. R. (2011). Estimating the effect of satellite orbital error
734 using wavelet-based robust regression applied to InSAR deformation data. *IEEE*
735 *Transactions on Geoscience and Remote Sensing*, *49*(11), 4600–4605.
736 Shirzaei, Manoochehr, Bürgmann, R., & Fielding, E. J. (2017). Applicability of Sentinel-1
737 Terrain Observation by Progressive Scans multitemporal interferometry for monitoring
738 slow ground motions in the San Francisco Bay Area. *Geophysical Research Letters*,
739 *44*(6), 2733–2742. https://doi.org/10.1002/2017GL072663
740 Shirzaei, Manoochehr, Freymueller, J., Törnqvist, T. E., Galloway, D. L., Dura, T., &
741 Minderhoud, P. S. J. (2021). Measuring, modelling and projecting coastal land
742 subsidence. *Nature Reviews Earth & Environment*, *2*(1), 40–58.
743 https://doi.org/10.1038/s43017-020-00115-x
744 Smith, C. M., & Graffeo, C. S. (2005). Regional Impact of Hurricane Isabel on Emergency
745 Departments in Coastal Southeastern Virginia. *Academic Emergency Medicine*, *12*(12),
746 1201–1205. https://doi.org/10.1197/j.aem.2005.06.024
747 Sopkin, K. L., Stockdon, H. F., Doran, K. S., Plant, N. G., Morgan, K. L., Guy, K. K., & Smith,
748 K. E. (2014). *Hurricane Sandy: observations and analysis of coastal change*. US
749 Department of the Interior, US Geological Survey.

Sweet, W. V., & Park, J. (2014). From the extreme to the mean: Acceleration and tipping points of coastal inundation from sea level rise. *Earth's Future*, *2*(12), 579–600. https://doi.org/10.1002/2014EF000272

Trochu, F. (1993). A contouring program based on dual kriging interpolation. *Engineering with Computers*, *9*(3), 160–177.

U.S. Census Bureau. (2021). U.S. Census Bureau QuickFacts: Portsmouth city, Virginia; Newport News city, Virginia; Norfolk city, Virginia; Virginia. Retrieved January 20, 2021, from https://www.census.gov/quickfacts/fact/table/portsmouthcityvirginia,newportnewscityvirginia,norfolkcityvirginia,VA/IPE120219

Wegnüller, U., Werner, C., Strozzi, T., Wiesmann, A., Frey, O., & Santoro, M. (2016). Sentinel-1 Support in the GAMMA Software. *Procedia Computer Science*, *100*, 1305–1312. https://doi.org/10.1016/j.procs.2016.09.246

Werner, C., Wegmüller, U., Strozzi, T., & Wiesmann, A. (2000). Gamma SAR and interferometric processing software. In *In Proceedings of the ers-envisat symposium gothenburg, Sweden* (Vol. 1620, p. 1620).